UNIVERSITY OF CALIFORNIA SAN DIEGO

Effects of Alterations in Sarcomere Structure and Prestretch Timing on Cardiac Muscle Mechanics

A thesis submitted in partial satisfaction of the requirements

for the degree Master of Science

in

Bioengineering

by

Jared Rylan Tangney

Committee in charge:

Professor Jeffrey H. Omens, Chair
Professor Andrew D. McCulloch, Co-Chair
Professor Richard L. Lieber

2012

The Thesis of Jared Rylan Tangney is approved and it is acceptable in quality and form for publication on microfilm and electronically:

Co-Chair

Chair

University of California, San Diego

2012

DEDICATION

To my parents, brothers, and soon to be wife, Monika.

EPIGRAPH

For wisdom is a defense as money is a defense, but the excellence of knowledge is that wisdom gives life to those who have it.

Ecclesiastes 7:12

TABLE OF CONTENTS

LIST OF FIGURES

LIST OF TABLES

ACKNOWLEDGEMENTS

I would first like to thank my advisors Dr. Jeff Omens and Dr. Andrew McCulloch. Their complementary yet unique styles of leading made for an environment that allowed me to excel in my academic and professional growth. All I have accomplished over these past few years would not have been possible without their guidance and patience.

I would also like to extend a special thanks to Stuart Campbell, who helped get my research off to a great start. Even after he moved on from UCSD, he was a constant source of guidance and support, helping shape my project into what it has become today.

I would like to thank all the members of CMRG for their support and help in my work. In particular I would like to thank Matt Janssen for his work in the vinculin study, Adarsh Krishnamurthy for his help with Continuity and for his work in developing the lattice mechanics model, Joyce Chuang for her initial work on the vinculin study, and William Auyeung, Shawn Sunu and Joseph Chung for their help in the papillary muscle experiments.

Lastly, I would like to thank my family. To my parents for offering a life for me that allowed me to focus on my education. To my brothers for always being there for support and when I need a good laugh. And lastly to my fiancé Monika, whose constant support and faith in me has enabled my growth, both professionally and personally.

Chapter 2, in part, is currently being prepared for submission for publication of the material. Tangney J; Campbell S; McCulloch AD; Omens JH. “Timing and Magnitude of Prestretch Affect Myofilament Activation.” The thesis author was primary investigator and author of this material.

Chapter 3, in full, is beign prepared for submission for publication of the material. Chuang J and Tangney J; Janssen M, Krishnamurthy A; Liao P, Hoshijima M; Zemljic-Harpf A; Ross R; Frank L; McCulloch AD; Omens JH. “Novel Role for Vinculin in Myocardial Fiber Mechanics and Heart Failure.” The thesis author was a primary investigator and co-first author of this material.

ABSTRACT OF THE THESIS

Effects of Alterations in Sarcomere Structure and Prestretch Timing on Cardiac Muscle Mechanics

by

Jared Rylan Tangney

Master of Science in Bioengineering

University of California, San Diego, 2012

Professor Jeffrey H. Omens, Chair

Professor Andrew D. McCulloch, Co-Chair

Changes in mechanical function in the heart have been shown to be associated with different mechanisms of heart failure. Mechanical function is disrupted in dyssynchronous heart failure, as the timing of contraction in altered in different regions of the heart, preventing a uniform contraction. This dyssynchrony can be simulated using regional ventricular pacing, which also alters mechanical function.

One purpose of the work presented here was to determine the effects of the altered cardiac muscle mechanics that arise due to regional ventricular pacing. It was found that a prestretch associated with dyssynchronous contraction can affect tension and work production in isolated cardiac muscle. The timing and magnitude of this stretch was also found to be of importance. Ultimately, the results could mostly be explained by a few well known muscle mechanics mechanisms: time-varying stiffness, the force-velocity relation, and shortening deactivation. Dilated cardiomyopathy (DCM) is another cause of heart failure, which can be brought about by mechanical dysfunction. The work presented here proposes a novel mechanism for contractile dysfunction associated with cardiac vinculin deletion, which is a precursor to dilated cardiomyopathy. It was shown that an increase in lattice spacing due to vinculin deletion increased transverse systolic stiffness and explains the altered systolic wall strains associated with vinculin deficiency. A combination of experiments, model development, and model simulation was used to uncover how changes in mechanical function associated with heart failure can alter cardiac muscle mechanics.

Chapter 1

General Introduction

1.1 DYSSYNCHRONOUS HEART FAILURE

It is a well-known fact that cardiovascular disease is a major medical problem in the United States, affecting over 80 million Americans[1]. The term cardiovascular disease includes many conditions such as high blood pressure, coronary heart disease, congenital cardiovascular defects, and heart failure; with the emphasis of this thesis being on heart failure. The 2011 American Heart Association estimate of the number of Americans with heart failure was over 5.7 million people, a number that is continuing to grow[1]. Heart failure is characterized by decreased pump function and the inability of the heart to supply adequate amounts of blood the body [2]. A standard of measuring pump function is ejection fraction, which is the percentage of end diastolic volume that is pumped out with each contraction. A healthy heart produces ejection fractions around 65% [3], while a failing heart has ejection fractions of less than 50% [4]. A common cause of the reduced pump function observed in heart failure is due to dyssynchronous activation of the myocardium, known as dyssynchronous heart failure, which is the motivation for the analysis performed in chapter 2.

Proper ejection of blood from the heart requires that a relatively synchronous contraction take place. Dyssynchronous contraction lacks the coordination required to efficient eject blood, leading to reduced pump function and heart failure. This dyssynchrony can arise from a conduction disturbance such as left bundle branch block (LBBB), which is the most common conduction disturbance in patients with advanced heart failure [5]. Another cause of dyssynchrony is myocardial infarction, where a scar is formed creating a region that no longer has the ability to contract. If the scar region is large enough, it can lead to dyssynchrony and left ventricular dysfunction [6].

A method used to simulate (in animal models) dyssynchrony observed in non-ischemic heart failure is epicardial ventricular pacing [7]. Ventricular pacing has also been shown to induce differences in regional workload which ultimately leads to regional hypertrophy [8]. This method of pacing has been shown to be a good model of the dyssynchrony induced due to LBBB, as the patterns of hypertrophy are similar [9].

1.2 LENGTH-DEPENDENT ACTIVATION

In order to study the effects of heart failure and how it comes about, it is important to understand the mechanical origins of failure at a much smaller scale than the whole organ. Muscle mechanics can be used to break down the mechanisms involved in heart failure; this analysis goes down to the subcellular level. If alterations

leading to or caused by heart failure can be understood at this subcellular level, it gives important insight into possible treatment or prevention.

The first aspect of muscle mechanics to be addressed, especially in the case of dyssynchronous heart failure due to the fact that the tissue undergoes varying degrees of stretch, is length-dependent activation. A well-known fact in muscle physiology is the dependence of contractile force on sarcomere length. A partial explanation for this relation involves myofilament overlap. As a cardiomyocyte is stretched, there is an increased amount of actin and myosin overlap, which allows for a greater number of myosin binding sites to be within range of the myosin heads. Myofilament overlap is most likely only a partial explanation of the Frank-Starling law of the heart, because the relationship between force produced and sarcomere length is much too steep and dependent upon contractile state to be explained entirely by myofilament overlap [10]. Experiments have shown that increasing sarcomere length seems to increase the affinity of TnC for calcium. This increased sensitivity to calcium at longer sarcomere lengths has also show to increase force development at same levels of activator calcium [11].

Changes in calcium sensitivity of the myofilament due to length change plays a large role in regulating force production. It is known that cardiac troponin-C (TnC) contains two high affinity calcium binding sites, and one low affinity binding site (different from skeletal muscle TnC which has two low affinity sites). The high affinity sites are always calcium-bound at normal physiological levels of calcium, but it is the low affinity site that accounts for the regulation of calcium and the activation

of the sarcomere [12]. The binding of calcium to this low affinity regulatory site causes the TnC to undergo a conformational change, exposing hydrophobic sites on its surface which then allow for interaction with TnI. TnI is known for its ability to interact with actin during low [Ca^{2+}] which in turn prevents the binding of myosin with actin, by a mechanism that is not completely understood. X-ray structural studies have shown data for the possibility of the movement of tropomyosin (Tm), caused by a conformational change in Tn due to Ca^{2+} binding, which exposes myosin binding sites. However, x-ray data also indicates that the movement of actin and Tn itself could be responsible for the exposure of the binding sites [12]. Either way, the steep relationship between available calcium and force production means that a cooperative mechanism is taking place, as calcium binding to one site on troponin most likely could not account for such a steep relationship. This cooperative manner is seen again once strong-binding of crossbridges takes place. Additional crossbridge binding is dramatically enhanced after strong binding, a cooperative mechanism that could have to do with the movement of Tm into an even more favorable position [11].

1.3 TIME-VARYING STIFFNESS

As muscle contracts, its mechanical properties change from those observed while in the passive state. The passive, viscoelastic properties of muscle make up a significant portion of total tension for a large range of sarcomere lengths, particularly below 1.85 μm and above 2.2 μm [13]. It has been shown that titin accounts for a large percentage of passive tension in the lower physiological range of sarcomere lengths, while collagen dominates at longer sarcomere lengths [14]. In addition to the

passive stiffness, when cardiac muscle contracts, the stiffness is increased. In particular, active stiffness dominates between sarcomere lengths of 1.85-2.2 μm, where it dominates over passive stiffness [13].

While titin and collagen are thought to dominate the passive stiffness of cardiac muscle, attached crossbridges determine the active stiffness. It has been shown that active stiffness is a good estimate of the total number of attached crossbridges [15]. What this means is that as more bridges are being recruited throughout the time-course of a twitch, the stiffness is increasing. This time-varying stiffness of cardiac muscle gives insight to describing the contractility of the tissue. In the whole heart, it was discovered that the time-varying elastance of the tissue was a good estimate of ventricular contractility [16].

1.4 FORCE-VELOCITY RELATION

The contractile force of cardiac muscle is highly dependent upon the rate of shortening [17]. Similar to skeletal muscle, maximum force production decreases with maximum shortening velocity; therefore maximum shortening velocity occurs under no load. A simple example of the force-velocity relation in action is the fact that a person can lift a light weight at much higher velocities than they can lift a heavy weight. This is because the forces needed to lift the heavier weight can only be generated at slower velocities. This relation between force and velocity is of high importance when analyzing the mechanics of isolated muscle.

Early cardiac muscle force-velocity curves were generated by varying the afterload on cat papillary muscles and observing the changes in shortening velocities [17]. Maximum shortening velocity in cardiac muscle has been shown to not be dependent upon sarcomere length (through physiological sarcomere length ranges), but does show some velocity dependence on the level of contractility due to external Ca^{2+} concentration [18]. These studies actually showed an increase in maximum shortening velocity with an increase in external Ca^{2+} concentration from 0.5 mM to 2.5 mM. This dependence of shortening velocity on Ca^{2+} is observed only in cardiac muscle, and not in skeletal muscle.

The exact mechanisms involved in describing the force-velocity relation are quite complex, so the basics will only be covered here. The most accepted reasoning behind the force-velocity relation involves rates of crossbridge binding and detaching. Due to the fact that there is a finite amount of time required for a crossbridge to bind, when muscle is shortening, the window of opportunity for the bridge to bind is decreased. It has been previously discussed that the number of bound crossbridges determines the amount of force produced, so if less bridges have time to bind due to shortening, the developed force will be decreased. An example of a quantitative crossbridge model of muscle contraction was based on the biochemical kinetic cycle for the actomyosin ATPase activity, and was able to predict experimental force-velocity curves [19].

There are documented effects of lengthening velocity on force production, although the reasoning behind this is of constant debate. It has been shown that with

an increased lengthening velocity (up to a certain amount), there is a marked increase in force production above that of the isometric case [20]. While the majority of the effects shortening velocity has on force production can be explained by crossbridge cycling theories, it appears that this is not the case for the effect of lengthening velocities on force production, where these theories are not sufficient [21]. While no exact mechanism has been uncovered, multiple possible theories have been published that give the most promising explanation to the phenomenon [22].

1.5 SHORTENING DEACTIVATION

Shortening-induced deactivation is a phenomenon that has been studied for decades, where shortening of a muscle actively producing force decreases the capacity to produce force and full force production is never restored [23]. The effect of shortening deactivation is dependent upon the magnitude of shortening, so increased shortening further inhibits recovery of contractile strength. The time during a twitch when shortening takes place has an effect on magnitude of deactivation. For example, induced shortening that takes place later in the twitch has been shown to increase the magnitude of deactivation, thus severely limiting the amount of redeveloped force after the length change has stopped [24]. The same study also showed that if the extracellular [Ca^{2+}] is increased, the deactivation due to shortening in minimized, showing the importance of calcium. Experiments have shown that the most likely cause of sustained deactivation is due to a reduction in affinity for calcium at TnC regulatory sites [25]. If the shortening is fast enough to detach crossbridges, then the rate of tension redevelopment is dependent on the concentration of bound calcium

[26]. Since the concentration of calcium bound to TnC decreases later in the twitch, this could explain why shortening deactivation has a greater effect later in the twitch.

1.6 LATTICE SPACING

Myosin and actin make up the thick and thin filaments, respectively. The sliding of these two filaments past each other during active contraction is the basis of the sliding filament theory, which describes how muscle contracts. The thick and thin filaments run along the fiber direction of muscle, and are arranged in parallel in a hexagonal shape, termed the lattice. The structure of the lattice is of importance because it determines how forces are distributed in 3-dimensions. Forces generated during contraction are not only directed axially, but they are distributed transverse to the fiber direction as well. Lattice spacing is generally reported either as the myosin-myosin spacing or actin-myosin spacing (center to center distance). It has been shown in both skeletal and cardiac muscle that myocytes maintain a resting volume that is constant. This constant volume implies that the lattice spacing is inversely proportion to the square root of the sarcomere length [27, 28].

Lattice spacing has been proposed to influence length-dependent activation because as the sarcomere is stretched, the myofilaments become closer together and lattice spacing is decreased, thus increasing the likelihood of crossbridge binding due to the myosin head being closer to the actin binding site. Experiments have been performed backing this hypothesis, showing how inter-filament spacing could influence filament activation [29]. A technique was used to alter inter-filament spacing

without changing sarcomere lengths. With these tests, the inter-filament spacing can be adjusted to match the spacing at a longer sarcomere length, and the resulting calcium sensitivity was tested. In performing these experiments using dextran, Fuchs and Smith concluded that calcium binding and sensitivity were correlated not with sarcomere length, but with a lateral separation between actin and myosin filaments [29]. As an attempt to confirm the proposed hypothesis, other groups performed a series of studies that ended up offering conflicting evidence to the inter-filament hypothesis. Konhilas and de Tombe performed a series of experiments in 2002 in which they were able to directly measure lattice spacing by synchrotron x-ray diffraction. They immersed cardiac trabeculae held at short sarcomere lengths (2.02 μm) in a concentration of dextran that reduced lattice spacing to that similar to long sarcomere lengths (2.19 μm). They found that compression due to dextran did not alter calcium sensitivity noticeably, whereas a stretch from 2.02 μm to 2.19 μm did increase calcium sensitivity considerably [30]. Higher concentrations of dextran did seem to increase calcium sensitivity, but that was most likely due to other effects of dextran rather than the change in lattice spacing [11]. The conclusion from this is that myofilament lattice spacing might not be the underlying mechanism behind length dependent activation of the myofilament, but its true role in activation is still controversial [11].

1.7 CROSSBRIDGE MECHANICS

Geometric models at the scale of the crossbridge can be used to describe the distribution of forces generated within a single bridge. When modeling a crossbridge

as a force producing structure, there are several different approaches that have been demonstrated. The most common approach has been to model the force generating segment as a spring. Traditionally this was developed as a spring that ran parallel to the myofilaments [31-33]. The problem with the single spring models which are oriented only in the axial direction, is that they neglect forces generated in the radial direction. While the axial spring models give insight into the forces generated in the fiber direction, they give no information about the radial component of force, which has been shown to be on the same order of magnitude as the fiber force [34, 35].

With evidence of radial forces of the same magnitude as axial forces, models were generated to include the radial component. These models must be 2 or 3-dimensional in order to factor in the radial component. An early example of a 3-dimensional crossbridge mechanics model was developed by Schoenberg [36, 37]. This model consisted of an S2 segment attached to myosin, and an S1 segment attached to actin, with S2 being the force generating segment. The model was geometrically based; so many angles were needed in order to fully resolve the model in 3-dimensions. A more recent model capable of resolving axial and radial forces was developed by Williams et al. [38]. They developed both a 2-spring model and a 4-spring model, where they incorporated torsional springs as well as linear springs. Both of these models have the ability to determine how the distribution of forces changes with a change in lattice spacing. This ability is of importance when incorporating crossbridge mechanics into models of contraction at the tissue scale, as the lattice helps determine distribution of forces in 3-dimensions.

1.8 SCOPE OF THE THESIS

The objective of chapter 2 of the thesis was to examine the effects of a physiological stretch observed during dyssynchronous contraction, termed “prestretch”. The effects of the timing and magnitude of prestretch on tension and work production were investigated. The muscle mechanics mechanisms needed to explain the results were investigated. The main mechanisms that were studied were length-dependent activation, time-varying stiffness, the force-velocity relation, and shortening deactivation. The study ultimately uncovered the effects of timing and magnitude of prestretch on tension and work production, as well as the essential mechanisms needed to explain these results.

The objective of chapter 3 of the thesis was to elucidate the function of vinculin in myocyte mechanics and regional ventricular wall motion. It has been shown that vinculin plays a structural role in ventricular myocytes and when disrupted, can lead to dilated cardiomyopathy and heart failure. It was hypothesized that vinculin deletion could affect lattice spacing and ultimately stiffness transverse to the myofibers. This hypothesis was investigated using a novel ventricular mechanics model, which was based on novel crossbridge mechanics and lattice mechanics models.

REFERENCES

1. Association, A.H., *Heart Disease and Stroke Statistics* 2011, American Heart Association: Dallas, TX.

2. Hunt, S.A., *ACC/AHA 2005 guideline update for the diagnosis and management of chronic heart failure in the adult: a report of the American College of Cardiology/American Heart Association Task Force on Practice Guidelines (Writing Committee to Update the 2001 Guidelines for the Evaluation and Management of Heart Failure).* J Am Coll Cardiol, 2005. **46**(6): p. e1-82.

3. Lorenz, C.H., et al., *Normal human right and left ventricular mass, systolic function, and gender differences by cine magnetic resonance imaging.* J Cardiovasc Magn Reson, 1999. **1**(1): p. 7-21.

4. Vasan, R.S., et al., *Congestive heart failure in subjects with normal versus reduced left ventricular ejection fraction: prevalence and mortality in a population-based cohort.* J Am Coll Cardiol, 1999. **33**(7): p. 1948-55.

5. Leclercq, C. and D.A. Kass, *Retiming the failing heart: principles and current clinical status of cardiac resynchronization.* J Am Coll Cardiol, 2002. **39**(2): p. 194-201.

6. Uusimaa, P., et al., *Collagen scar formation after acute myocardial infarction: relationships to infarct size, left ventricular function, and coronary artery patency.* Circulation, 1997. **96**(8): p. 2565-72.

7. Faris, O.P., et al., *Endocardial versus epicardial electrical synchrony during LV free-wall pacing.* Am J Physiol Heart Circ Physiol, 2003. **285**(5): p. H1864-70.

8. van Oosterhout, M.F., et al., *Asynchronous electrical activation induces asymmetrical hypertrophy of the left ventricular wall.* Circulation, 1998. **98**(6): p. 588-95.

9. Prinzen, F.W., et al., *Asymmetric thickness of the left ventricular wall resulting from asynchronous electric activation: a study in dogs with ventricular pacing and in patients with left bundle branch block.* Am Heart J, 1995. **130**(5): p. 1045-53.

10. Konhilas, J.P., T.C. Irving, and P.P. de Tombe, *Frank-Starling law of the heart and the cellular mechanisms of length-dependent activation.* Pflugers Arch, 2002. **445**(3): p. 305-10.

11. de Tombe, P.P., et al., *Myofilament length dependent activation.* J Mol Cell Cardiol, 2010. **48**(5): p. 851-8.

12. Kobayashi, T. and R.J. Solaro, *Calcium, thin filaments, and the integrative biology of cardiac contractility.* Annu Rev Physiol, 2005. **67**: p. 39-67.

13. Hunter, P.J., A.D. McCulloch, and H.E. ter Keurs, *Modelling the mechanical properties of cardiac muscle.* Prog Biophys Mol Biol, 1998. **69**(2-3): p. 289-331.

14. Granzier, H.L. and T.C. Irving, *Passive tension in cardiac muscle: contribution of collagen, titin, microtubules, and intermediate filaments.* Biophys J, 1995. **68**(3): p. 1027-44.

15. Ford, L.E., A. F. Huxley, and R. M. Simmons, *The relation between stiffness and filament overlap in stimulated frog muscle fibres.* J. Physiol. , 1981(311): p. 219–249.

16. Suga, H., K. Sagawa, and A.A. Shoukas, *Load independence of the instantaneous pressure-volume ratio of the canine left ventricle and effects of epinephrine and heart rate on the ratio.* Circ Res, 1973. **32**(3): p. 314-22.

17. Sonnenblick, E.H., *Force-velocity relations in mammalian heart muscle.* Am J Physiol, 1962. **202**: p. 931-9.

18. Daniels, M., et al., *Velocity of sarcomere shortening in rat cardiac muscle: relationship to force, sarcomere length, calcium and time.* J Physiol, 1984. **355**: p. 367-81.

19. Eisenberg, E., T.L. Hill, and Y. Chen, *Crossbridge model of muscle contraction. Quantitative analysis.* Biophys J, 1980. **29**(2): p. 195-227.

20. Joyce, G.C., P.M. Rack, and D.R. Westbury, *The mechanical properties of cat soleus muscle during controlled lengthening and shortening movements.* J Physiol, 1969. **204**(2): p. 461-74.

21. Harry, J.D., A. W. Ward, N. C. Heglund, D. L. Morgan, and T. A. McMahon, *Crossbridge cycling theories cannot explain high-speed lengthening behavior in frog muscle.* Biophys. J., 1990. **57**: p. 201-208.

22. Morgan, D.L., *New insights into the behavior of muscle during active lengthening.* Biophys J, 1990. **57**(2): p. 209-21.

23. Edman, K.A., *Mechanical deactivation induced by active shortening in isolated muscle fibres of the frog.* J Physiol, 1975. **246**(1): p. 255-75.

24. Kaufmann, R.L., R.M. Bayer, and C. Harnasch, *Autoregulation of contractility in the myocardial cell. Displacement as a controlling parameter.* Pflugers Arch, 1972. **332**(2): p. 96-116.

25. Edman, K.A., *Fatigue vs. shortening-induced deactivation in striated muscle.* Acta Physiol Scand, 1996. **156**(3): p. 183-92.

26. Peterson, J.N., W.C. Hunter, and M.R. Berman, *Estimated time course of Ca2+ bound to troponin C during relaxation in isolated cardiac muscle.* Am J Physiol, 1991. **260**(3 Pt 2): p. H1013-24.

27. Pearson, J.T., et al., *In situ measurements of crossbridge dynamics and lattice spacing in rat hearts by x-ray diffraction: sensitivity to regional ischemia.* Circulation, 2004. **109**(24): p. 2976-9.

28. Irving, T.C., et al., *Myofilament lattice spacing as a function of sarcomere length in isolated rat myocardium.* Am J Physiol Heart Circ Physiol, 2000. **279**(5): p. H2568-73.

29. Fuchs, F. and S.H. Smith, *Calcium, crossbridges, and the Frank-Starling relationship.* News Physiol Sci, 2001. **16**: p. 5-10.

30. Konhilas, J.P., T.C. Irving, and P.P. de Tombe, *Myofilament calcium sensitivity in skinned rat cardiac trabeculae: role of interfilament spacing.* Circ Res, 2002. **90**(1): p. 59-65.

31. Huxley, A.F., *Muscle structure and theories of contraction.* Prog Biophys Biophys Chem, 1957. **7**: p. 255-318.

32. Daniel, T.L., A.C. Trimble, and P.B. Chase, *Compliant realignment of binding sites in muscle: transient behavior and mechanical tuning.* Biophys J, 1998. **74**(4): p. 1611-21.

33. Chase, P.B., J.M. Macpherson, and T.L. Daniel, *A spatially explicit nanomechanical model of the half-sarcomere: myofilament compliance affects Ca(2+)-activation.* Ann Biomed Eng, 2004. **32**(11): p. 1559-68.

34. Cecchi, G., et al., *Detection of radial crossbridge force by lattice spacing changes in intact single muscle fibers.* Science, 1990. **250**(4986): p. 1409-11.

35. Millman, B.M., *The filament lattice of striated muscle.* Physiol Rev, 1998. **78**(2): p. 359-91.

36. Schoenberg, M., *Geometrical factors influencing muscle force development. I. The effect of filament spacing upon axial forces.* Biophys J, 1980. **30**(1): p. 51-67.

37. Schoenberg, M., *Geometrical factors influencing muscle force development. II. Radial forces.* Biophys J, 1980. **30**(1): p. 69-77.

38. Williams, C.D., M. Regnier, and T.L. Daniel, *Axial and radial forces of crossbridges depend on lattice spacing.* PLoS Comput Biol, 2010. **6**(12): p. e1001018.

Chapter 2

Timing and Magnitude of Prestretch Affect Myofilament Activation

2.1 INTRODUCTION

Asynchronous activation of the heart due to a conduction disturbance such as left bundle branch block (LBBB) has been recognized as a risk factor for the development of heart failure [1]. Currently, the most promising therapy for patients with conduction disturbances is cardiac resynchronization therapy (CRT). As promising as this approach is for some patients, CRT still poses some problems, as its effect on the electro-mechanics of the heart is not completely understood. During regional ventricular pacing, early contraction can be seen near pacing sites, which then causes a contraction wave-front to propagate to the opposite side of the heart [1-4]. Contraction of early-activated regions stretches other areas of the heart that have not yet been activated [1]. The stretching of late-activated regions by early-activated shortening has been previously referred to as “prestretch” [3, 5, 6], with Badke et al. being among the first to recognize prestretch [3]. The stretch has been shown to reach magnitudes of up to 20% in late-activated regions [4]. Due to the significant magnitude of prestretch, it is thought to have an impact on both acute and chronic myocardial function, and may affect long-term load-dependent remodeling responses.

Previous studies have concluded that asynchronously contracting hearts undergoing regional ventricular pacing have regions of external work imbalance [7, 8]. These studies showed that early-activated regions produced significantly less external work than late-activated regions. It was also shown that there was a significant difference between early and late-activated regions in terms of the amount of oxygen uptake and myocardial blood flow [8]. Observed imbalances in workload have been shown to play a role in asymmetrical hypertrophy, where early-activated LV free wall becomes significantly thinner and late-activated septum becomes significantly thicker [9]. The largest magnitude of prestretch is observed in late-activated regions [2], and could potentially have an effect on the external work developed by the region, leading to implications for remodeling.

The effects of prestretch on acute mechanical function and long-term remodeling of cardiac muscle are not thoroughly understood. The first aim of this study was to investigate the acute mechanical effects of prestretch, as a means of giving insight into its possible long-term impact on mechanical function and remodeling. The second aim of this study was to understand the key mechanisms involved in tension responses to realistic patterns of prestretch. To achieve this, isolated mouse right ventricular (RV) papillary muscles were stretched to mimic the magnitude, timing, and duration of prestretch observed in dog hearts *in-vivo* [2]. Different regions of the heart experience varying timings and magnitudes of prestretch, so the effects of these two variables on twitch tension were investigated. Due to the apparent role of workload in asynchronous hypertrophy, the effects of

prestretch on external work were also studied. One of the benefits of using an isolated muscle preparation was that the fiber stress – fiber strain area could be measured directly, due to the fact that fiber stress could be measured instead of approximated as is done *in-vivo* [8].

The present study differs from the many isolated muscle stretch studies found in the literature that make use of non-physiological stretches (i.e. non-physiological velocities, magnitudes, or durations). While these studies are important, they do not directly inform our understanding of *in-vivo* prestretch, its effects on tension development and myofilament activation, and its underlying mechanisms. It is currently not well understood exactly which mechanisms are most important in describing the effects of a transient stretch such as prestretch, and with the impact prestretch has on acute mechanical function, these mechanisms are important to understand.

2.2 METHODS

2.2.1 Muscle Isolation and Mounting

All experimental procedures were carried out in accordance to AAALAC guidelines and the guidelines for the care and use of laboratory animals of the University of California of San Diego. Male 129/SvJ mice were anesthetized using isoflurane, followed by cervical dislocation. The chest of the animal was then opened up and the heart was arrested via intra-cardiac injection of a cardioplegic solution described in table 2.1. The heart was then rapidly excised, canulated, placed in a bath with the cardioplegic solution, and retrogradely perfused through the aorta with the same solution. Incisions were then made in the right ventricular free wall to allow for access to the RV papillary muscles. Long, un-branched papillary muscles were dissected and used for the study.

Table 2.1: Modified Krebs-Henseleit Solution used to perfuse tissue, with the bottom two components added for use in the cardioplegic solution.

Modified Krebs-Henseleit Solution
141 mM NaCl
5mM KCl
1mM $MgSo_4$
1.2 mM NaH_2PO_4 (anhydrous)
25 mM $NaHCO_3$
5mM HEPES*
2mM $CaCl_2$*$2H_2O$
25mM KCl
Added for arrest solution:
25mM KCl
20nM 2,3-BDM

The selected papillary muscle was then placed in a muscle chamber (model 801C, Aurora Scientific, Inc.) mounted on an inverted microscope (Nikon Eclipse TE300). The septal end of the muscle was attached to a force transducer (model 405A, Aurora Scientific, Inc.) and the chordae tendineae was pierced with a hook attached to a high-speed, servo controlled lever arm (model 322C, Aurora Scientific, Inc.). The muscle chamber was constantly perfused with a modified Krebs-Henseleit solution (pH 7.35) bubbled with 95% oxygen and 5% CO_2 in a reservoir, immediately prior to being gravity fed into the muscle chamber. A peristaltic pump was used to pump the perfusion solution out of the chamber and was recycled back into the reservoir chamber.

Once the muscle was mounted in the chamber, a specific protocol was followed for each experiment. The muscle was paced at a desired frequency using platinum electrodes mounted inside the chamber. Each muscle was allowed to

equilibrate for at least 30 minutes or until it was able to pace steadily. All stretching was imposed using the computer-controlled high-speed motor with the attached hook.

2.2.2 Strain Tracking

Strain tracking was performed during most experiments. Titanium dioxide particles were sprinkled on the surface of the muscle, and were used as markers to track strain. A high speed CCD camera (model IP-VGA210, Imprerx, Inc.) was used to track markers during stretch and contraction at frame rates of up to 300 fps. The timing of the images was synchronized with force data obtained during the experiments. A MATLAB script was written to track the markers in the images and was used to calculate the strain between images. After running the script, data for both stress and strain throughout the course of the experiment was available for analysis.

2.2.3 Calcium Imaging

Calcium imaging was also performed on a subset of the muscles tested. The ratiometric fluorescent dye, Fura-2AM, was used to obtain calcium transients during experiments. The fluorophore was excited at both 340 nm (Ca^{2+} saturated) and 380 nm (Ca^{2+} free) and the ratio of the two is directly related to the amount of free intracellular calcium. The Fura-2AM was added to a loading solution that is described in table 2.2. The loading solution was then poured into the empty muscle chamber in a dark room, where it was allowed to load for 30 minutes. After the dye had sufficient time to penetrate cell membranes, the chamber was flushed with perfusion solution to rid the chamber of excess dye. The experiment then proceeded with the predetermined

protocol, and throughout the course of the experiment, the muscle was subjected to alternating 340nm and 380nm light via a fast filter switcher (Lambda DG-4, Sutter Instrument, Inc.) and the ratiometric measurement of fluorescence was captured using a photomultiplier tube system (PMT-100, Applied Scientific Instrumentation).

Table 2.2: Calcium loading solution used for calcium imaging.

Calcium Loading Solution	
50 μL 1mg/mL fura-2	15 μL cremophor EL
25 μL 20% w/v Pluronic F-127	30 μL 100X TPEN stock (0.43 mg/mL)
125 μL H_2O	2.755 mL perfusate (pre-oxygenated)

2.2.4 Prestretch Protocol

A protocol was designed to investigate the effects of the timing and magnitude of prestretch on tension production. Precise control of the stretch timing is crucial in order to observe its effects. A computer program was written to aid in the user control and reproducibility of the experiments. This program allowed for the definition of exact magnitude, duration, timing, and shape of the desired stretch. The prestretch protocol consisted of 30 differently timed stretches, where the timing of the stretch was altered with respect to stimulation time. Stimulation time was 150 ms into a beat, where the cycle length was 500 ms (2 Hz pacing rate). Each stretch had a duration of 150ms, with a half sinusoidal lengthening and shortening, as can be seen in figure 2.1.

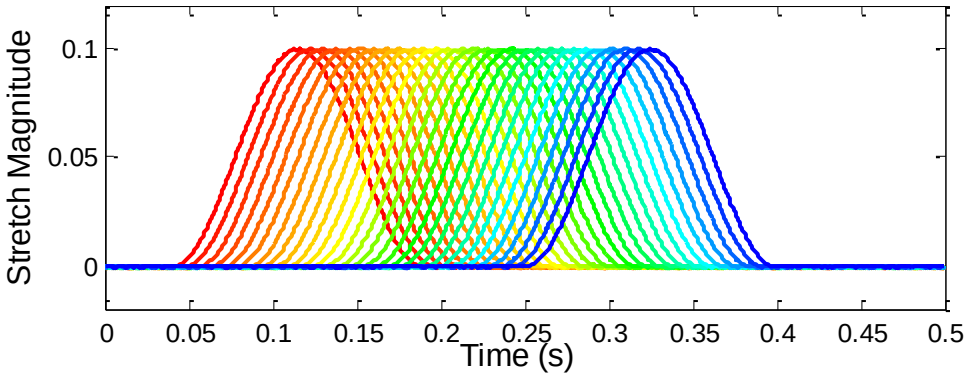

Figure 2.1: The timing and magnitude of stretches imposed on papillary muscles. The magnitude shown as the fraction of resting length (~2µm). Stimulation time is shown as the vertical dashed line (150ms).

The timing of the stretches was not only varied, but the magnitude was changed as well. 5%, 10%, and 15% of total muscle length stretches were applied to the muscles for each timing of stretch. These magnitudes were chosen as they fall within the range of prestretch observed *in-vivo* [4]. A CCD camera was calibrated to determine pixel size, and was used to determine the length of the muscles as well as the cross sectional area which was then used to calculate tension from force values.

The experiments were broken down into beats, with 3 different possible types of beats: an isometric beat, an actively stretched beat, and a passively stretched beat. An isometric beat is one that is stimulated and not stretched, where the overall muscle length is held constant. An actively stretched beat is one where the muscle is stimulated normally and one of the stretches seen in figure 2.1 is applied to the muscle at some defined time. A passively stretched beat is one where the same stretch is applied, but the muscle is not stimulated, so the passive tension produced due to

stretch is measured. If the passive tension is subtracted from the total tension in the stretched beat, what is left is the active tension.

Multiple beats were organized into sequences, where a sequence consisted of seven beat intervals of equal duration. The first five were isometric beats, followed by one actively stretched beat and one passively stretched beat. The stretched and passive beats in the same sequence always contain the same stretch. The isometric beats at the beginning of each sequence are designed to allow the muscle to recover from a stretch, so the effects of stretch do not propagate to following stretched beats. Figure 2.2 shows an example of one sequence of beats. In an experiment, many of these sequences are arranged to take place back to back, with each sequence containing a differently timed stretch.

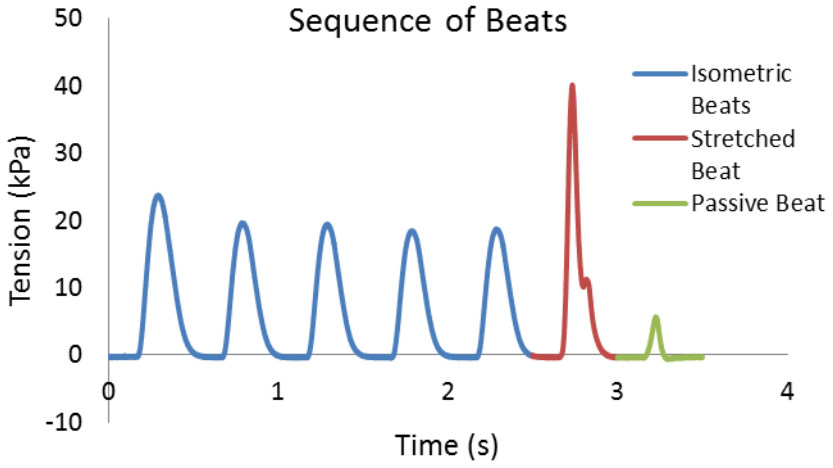

Figure 2.2: Sequence of beats consisting of 5 isometric beats followed by a stretched beat and a passive beat.

2.2.5 Time-varying stiffness Protocol

To aid in the analysis of the effects of prestretch on twitch tension production, measured values of muscle stiffness throughout the time-course of a beat were acquired. The instantaneous stiffness (S) was measured at 30 different time points throughout the time-course of a twitch. This was done by performing step stretches with a magnitude of 10% of total muscle length at each desired time point during a twitch. The strain (ε) placed on the muscle due to the step stretch was measured using the topical markers and a CCD camera as explained previously, while the change in tension (T) due to the step stretch was measured using the force transducer. With both the instantaneous change in strain and tension due to the stretch, the instantaneous stiffness was calculated using the following equation [10]:

$$S = \frac{\Delta T}{\Delta \varepsilon} \qquad [2.1]$$

With the known stiffness at 30 different time points throughout a twitch, this data was then used to calculate the estimated tension time-course due to time-varying stiffness. This was done by taking the measured stiffness time-course and multiplying it by the strain imposed on the muscle by a defined prestretch:

$$T_{TVS} = S \times \varepsilon_{PS} = \frac{\Delta T}{\Delta \varepsilon} \times \varepsilon_{PS} \qquad [2.2]$$

The result is an estimated twitch tension due to time-varying elastance (T_{TVS}) from an imposed prestretch strain (ε_{PS}).

2.3 RESULTS

2.3.1 Simulating Prestretch

In order for this study to give insight to the effects of prestretch *in-vivo*, realistic stretches of physiological timing, magnitude, and duration were imposed on mouse papillary muscles. The duration, maximum magnitude, and time-course of the stretches performed were designed based on prestretch observed in dogs subjected to regional ventricular pacing [2], and initial results show that the duration and magnitude of the stretch produce strains similar to what is observed *in-vivo* (figure 2.3). Variably timed stretches were performed as a means to examine the effects of the timing of prestretch on tension production.

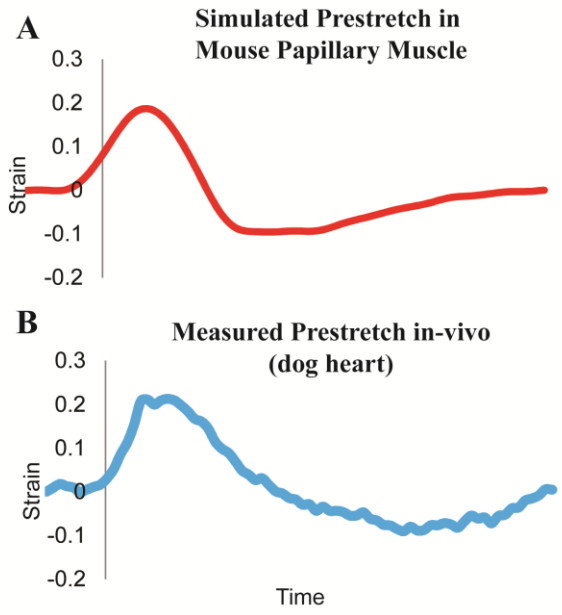

Figure 2.3: (A) Measured strain from simulated prestretch in mouse papillary muscle. (B) Measured in-vivo strain from prestretch induced by regional ventricular pacinpg [2].

2.3.2 Effects of Stretch Timing

Timing of prestretch varies in different regions of the heart, depending on the distance from the pacing site [7]. Due to the variability of the timing of prestretch in different regions of the heart, it is important to understand how this difference in timing alters contractility. In an initial attempt to investigate the effects of prestretch timing, 5 stretches with variable timing (in relation to stimulation) were performed on mouse papillary muscles (n=5). The results of these experiments showed a significant effect ($p<0.05$) of stretch timing on peak tension production. Figure 2.4 shows the twitch tension time-courses for 5 different prestretch timings, varied in relation to time of stimulation.

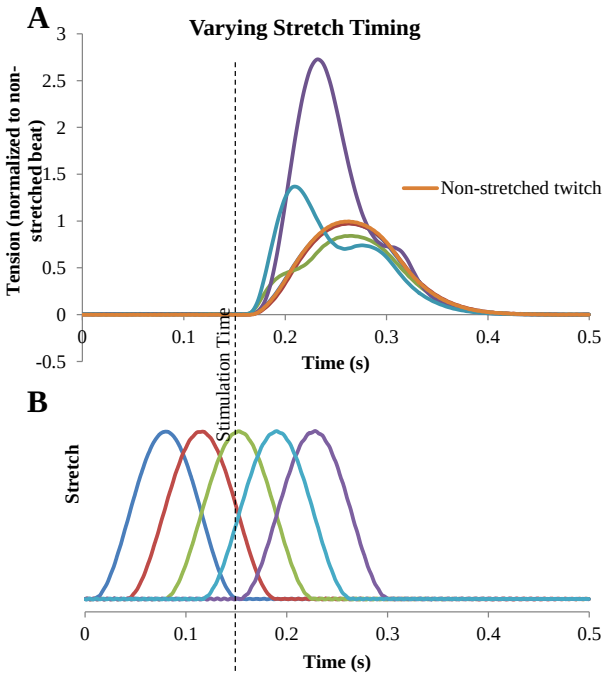

Figure 2.4: 5 stretches with their timing varied in relation to stimulation (dashed line). (A) Tension trace color matches corresponding stretch trace color. (B)The corresponding stretches.

The figure shows the pronounced effect of the timing of prestretch on tension production. The first two stretches do not have much of an effect on twitch tension (traces are obscured by that of the isometric beat). The timing of the third stretch shows an inhibitory effect on tension production, as the peak is lower than the peak for the non-stretched beat. The fourth stretch shows an increase in tension well above that of a non-stretched twitch, then dips back down lower as the stretch finishes. The latest stretch exhibits the largest increase in peak tension.

The initial set of experiments showed that stretch timing is highly influential in both the peak tension produced and the tension time-course. More resolution on the effect of stretch timing was desired, so a set of experiments was designed that utilized 30 different stretches, each separated by 7.5 ms. The results from these experiments

(figure 2.5) gave a more detailed understanding of the effects of timing through the desired interval, allowing for comparison to prestretch observed *in-vivo*.

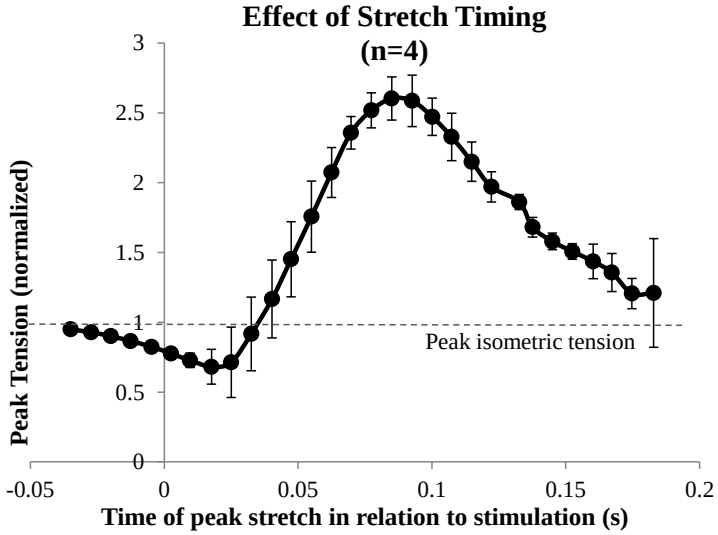

Figure 2.5: Peak tensions produced by 30 different prestretches. x-axis corresponds to timing of peak stretch, while the y-axis corresponds to peak tension resulting from that stretch, normalized to the peak tension of a non-stretched beat.

The x-axis timing corresponds to the peak timing of the prestretch. The figure shows that there is an interval where prestretching inhibits peak tension production. Stretches peaking at the time of stimulation to 25 ms after stimulation, show a decrease in peak tension of at least 25%. It isn't until 40 ms after stimulation do the peak tensions return to isometric values. On the contrary, there is also an interval of stretch timing that drastically increases peak twitch tension. The interval of stretches peaking 60 ms after stimulation to 125 ms after stimulation show increases in peak tension of at least 200%.

2.3.3 Effects of Stretch Magnitude

Papillary muscles were stretched to magnitudes of 5%, 10%, and 15% of total muscle length to simulate the possible range of stretch magnitudes observed *in vivo* [4]. There were 5 variably timed stretches at these 3 magnitudes, and the results from these experiments can be seen in figure 2.6.

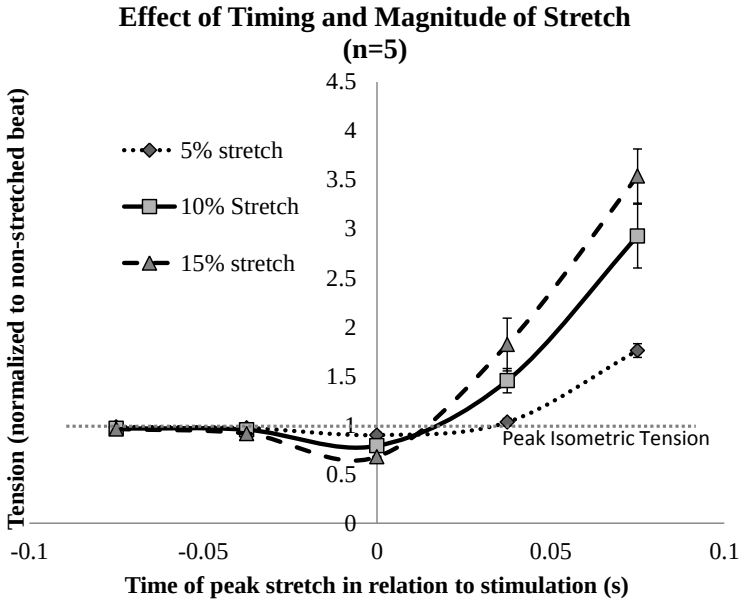

Figure 2.6: 5 different prestretches at 3 different magnitudes. x-axis corresponds to peak timing of stretch, with time=0 corresponding to stimulation, while y-axis values are peak tension normalized to non-stretched beat.

The figure shows that the influence of the magnitude of stretch is highly dependent on the timing of the stretch, with some stretches being greatly influenced by stretch magnitude, and others not as much. The first two stretches appear to be influenced very little by stretch magnitude. The third stretch (peak of stretch during stimulation) shows that with an increase in stretch magnitude, there is a decrease in peak tension production. An example of a stretch that inhibits peak tension can be seen in figure 2.7.

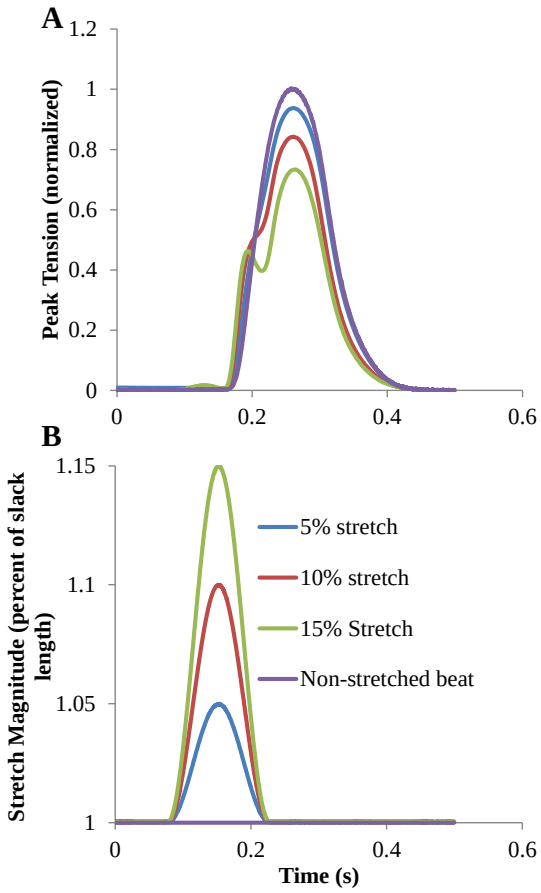

Figure 2.7: Example of a timing of prestretch that inhibits peak tension production. 3 different magnitudes of stretch (B) and corresponding tension production (A).

The results show that the stretch not only alters the magnitude of peak tension, but also influences the tension time-course. The fourth and fifth stretches in figure 2.6 (peak of stretches occurring after stimulation) show that an increase in stretch magnitude increases tension production (figure 2.8).

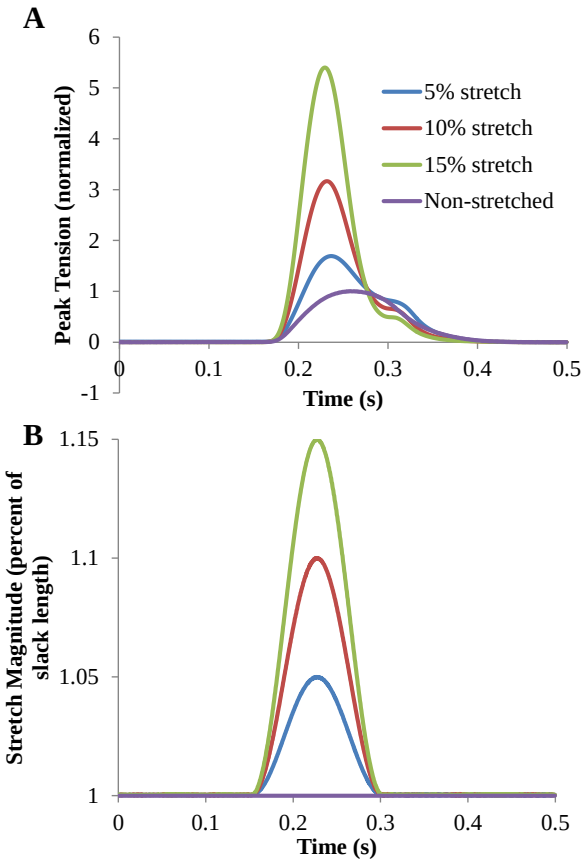

Figure 2.8: Example of a timing of prestretch that amplifies peak tension production. 3 different magnitudes of stretch (B) and corresponding tension production (A).

2.3.4 Effects of Prestretch on Work

The ability of the muscle to do work is an important quantity to measure, as it helps to translate results from the tissue scale to the whole heart scale. Work is measured here as the fiber stress-fiber strain area, as is done in the intact heart *in-vivo* [8]. Since the strain is measured in the center of the muscle, this is the external work the center of the muscle is doing on both ends of the tissue, because the ends are

stretched when the center contracts. Figure 2.9 shows that stretches peaking 50-125 ms after stimulation do much more work than other stretches. This indicates that stretch timing plays a large role in the amount of external work done by the muscle.

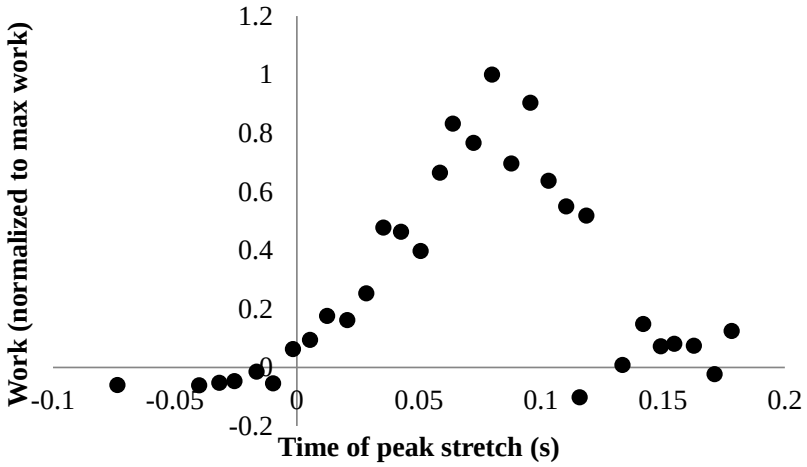

Figure 2.9: Work generated for a given timing of prestretch, normalized to max work.

2.3.5 Time-Varying Stiffness

To determine the role of time-varying stiffness in the prestretch results, a series of step-stretches were performed to determine the instantaneous stiffness throughout a twitch. Figure 2.10 shows the stiffness values obtained from this experiment plotted on top of an isometric beat (scaled equally to show correlation in timing).

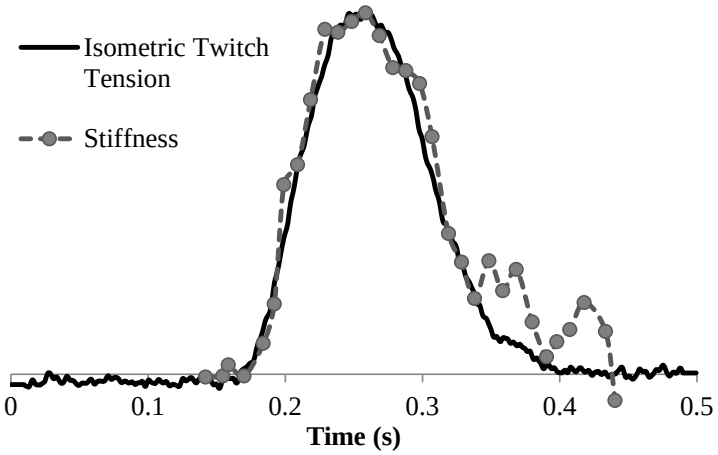

Figure 2.10: Measured instantaneious stiffness values plotted on top of isometric twitch, showing stiffness increases with twitch tension.

The results show that the peak stiffness of the muscle corresponds with the peak twitch tension of a non-stretched beat.

The stiffness results were compared to the results from the varied stretch timing experiments. The comparison between the peak tensions produced during each stretch is compared to an isometric twitch in figure 2.11.

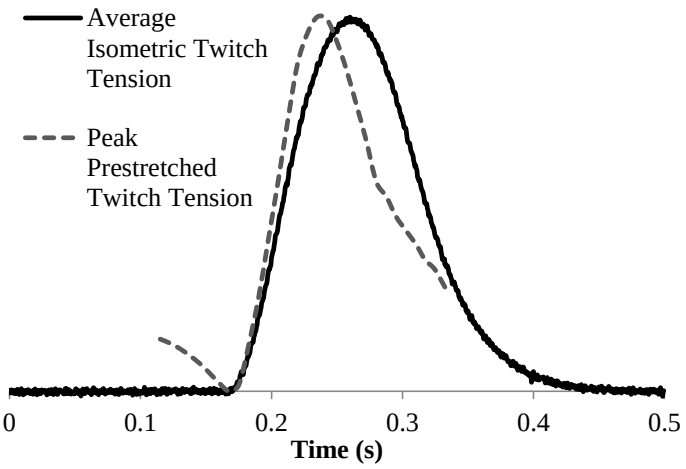

Figure 2.11: Peak prestretched twitch tension from figure 2.5 plotted on top of an isometric twtich (estimation of time-varying stiffness) to show peak prestretched tension does not correlate with peak stiffness.

The isometric twitch represents the stiffness time-course (as they are the same), and the dashed line is the data from figure 2.5, scaled to show the timing differences between the peaks. Figure 2.11 shows that the stretch that produced the most peak tension occurred prior to when the muscle was at its peak stiffness.

The measured stiffness values were used to predict the change in tension due to the time-varying stiffness using equation 2.2. The results from these calculations can be seen in panel A of figure 2.12.

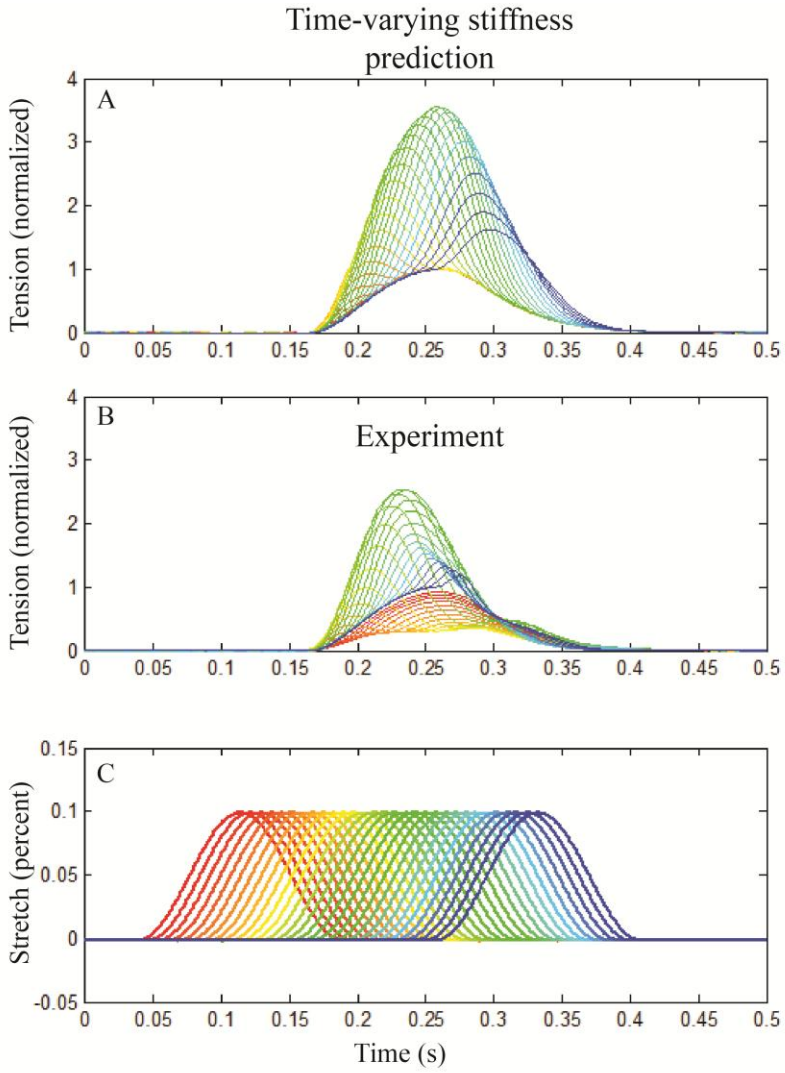

Figure 2.12: (A) Time-varying stiffness prediction of twitch tension due to prestretch. (B) Twitch tension from experimental prestretch. (C) Time-courses of the 30 different prestretches.

It should be noted that peak tension values, the timing of the stretches producing the most tension, and the peak tension inhibition that is seen in the prestretch results is not replicated by time-varying stiffness alone. The peak tensions produced by prestretch experiments and the analysis done using time-varying elastance were compared (figure 2.13).

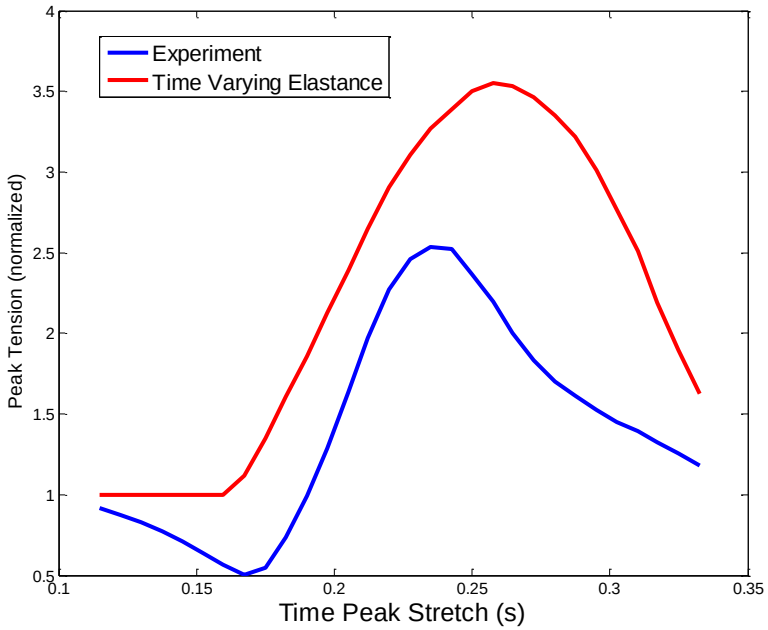

Figure 2.13: Peak tensions as predicted by time-varying stiffness (red trace) and the experimental peak tension values due to prestretch (blue trace). x-axis refers to time of peak prestretch.

This figure emphasizes the differences between the experimental prestretch results and the analysis done using time-varying stiffness alone. The prestretch results in figure 2.13 were subtracted from the time-varying stiffness results in the same figure to get a difference in the two curves, showing for which stretches the time-varying stiffness analysis produced the largest discrepancies with experimental results (figure 2.14).

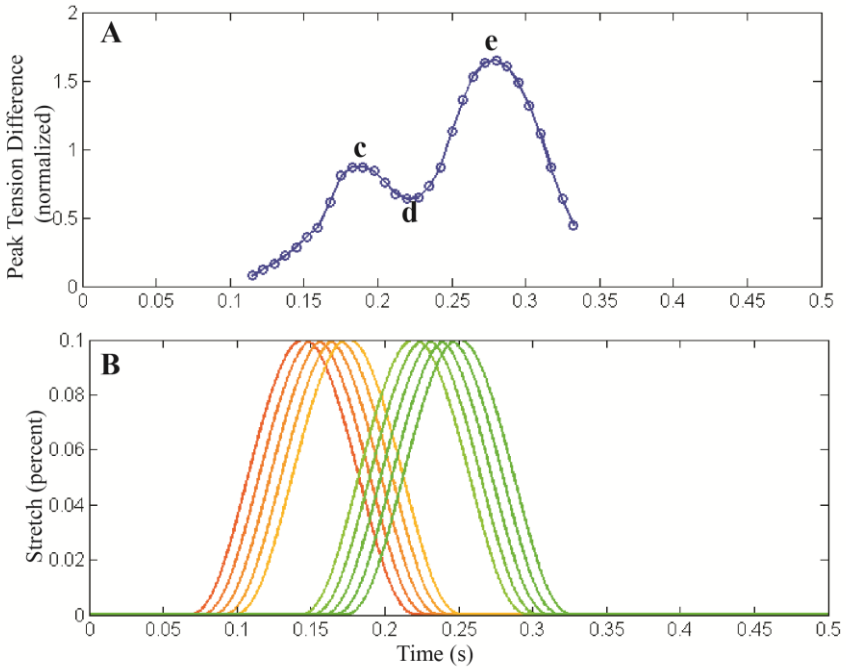

Figure 2.14: (A) Experimental prestretched peak twitch tension subtracted from time-varying stiffness predicted peak tensions for same timing of prestretch. (B) First 5 stretches correspond to prestretches producing the least peak tension, and last 5 stretches correspond to prestretches producing the highest peak tension.

There are two separate regions where time-varying stiffness alone predicts tensions much higher than what is seen experimentally (labeled as **c** and **e** in the figure). Between these two regions, there is an interval where the time-varying stiffness analysis drops down closer to that of the experiments (**d**). The difference between the two curves is a good way of determining where the time-varying elastance alone cannot explain the results, so further analysis is needed.

2.3.6 Effects of Velocity on Peak Tension

The effects of maximum shortening and lengthening velocity of prestretch on peak tension production were analyzed. Figure 2.15 shows that stretches with maximum lengthening velocity occurring near the peak of the calcium transient produced the highest peak active tensions.

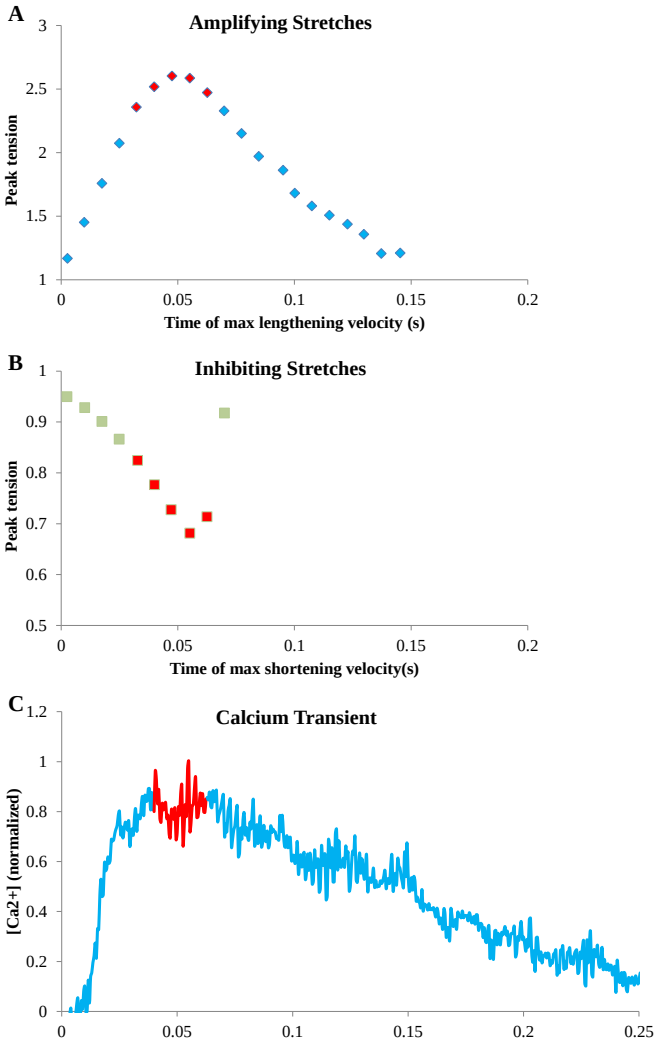

Figure 2.15: (A) Peak tensions produced by amplifying prestretches plotted as a function of maximum lengthening velocity of the stretch. (B) Peak tensions produced by inhibiting prestretches plotted as a function of maximum shortening velocity of the stretch. (C) Calcium transient showing peak inhibiting and amplifying prestretches (red markers in panels A and B) correlate with the peak of the calcium transient (red section of trace in panel C).

Stretches with maximum shortening velocity occurring near maximum free calcium concentration correlate to twitches that produce the greatest decrease in peak tension, below that of a non-stretched beat.

The effects of velocity were analyzed by looking at individual twitches. An example of this can be seen in figure 2.16, where two stretches were selected for analysis: panel C being the stretch that produces the least peak tension (less than that of a non-stretched beat), and panel F being the stretch that produces the most peak tension.

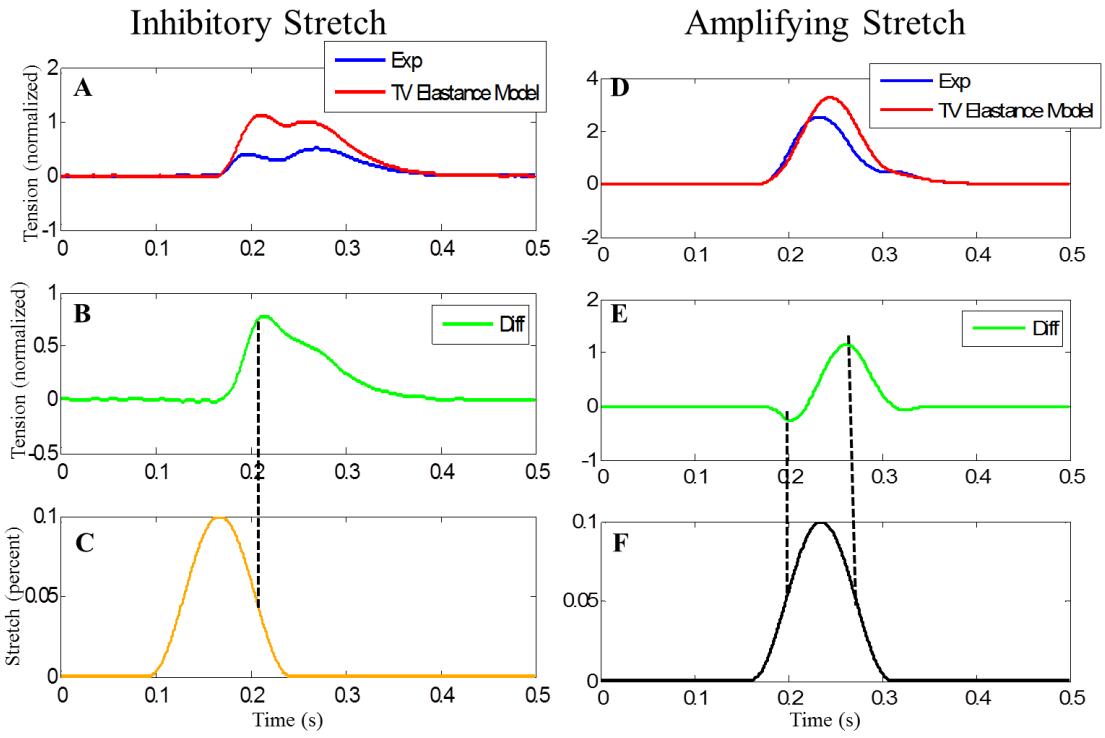

Figure 2.16: (A,D) Experimental twitch (blue trace) and time-varying stiffness predicted twitch tension (red trace). (B,E) Difference between time-varying elastance prediction and experimental twitch tension. (C,F) Prestretch for individual beat.

These stretches were compared to the time-varying stiffness prediction for that same stretch, and the differences are shown in panels B and E. The dashed line between panels B and C shows that the peak difference occurs during maximum shortening velocity of the prestretch. The first dashed line between panels E and F shows that the time-varying stiffness prediction underestimates the tension during maximum lengthening velocity of the prestretch. The second dashed line between panels E and F shows that the peak difference occurs during maximum shortening of the prestretch.

2.4 DISCUSSION

In this study, the effects of timing and magnitude of prestretch on developed twitch tension in mouse papillary muscles were measured using a computer controlled isolated muscle stretching system. The results of the study show that the twitch tension and work performed by the muscle are highly dependent on the timing and magnitude of prestretch. A time-varying stiffness analysis was performed to break down the mechanisms involved in the results. While this analysis made it clear that the stiffness change during contraction did have a substantial effect on the twitch tension, it could not fully explain the results. Further analysis of the results suggested that the force-velocity relationship could help explain much of the results that could not be explained by the time-varying stiffness analysis. Other mechanisms that can possibly explain some of the more minor differences are discussed in greater detail to come.

2.4.1 Effects of Stretch Timing

This study shows that prestretch timing has a significant effect on tension production. The timing results are of importance because different regions of the heart experience prestretch at different times in relation to local tissue activation. It is no surprise that prestretch affects tension production in cardiac muscle, as length dependent activation has been studied by many [11] and it is known that stretch increases the affinity of troponin C for calcium and increases cross-bridge formation [12]. Even with this well-known phenomenon, to our knowledge, the effects of

prestretch on tension production have never been studied in isolated cardiac tissue. The ability to have precise control over stretch timing, magnitude, and shape was made possible by the advanced computer controlled system, designed for these experiments.

The experimental results of this study are complex in nature and cannot be explained by a simple mechanism. If simply the Frank-Starling law were considered, muscles stretched to longer lengths during activation would be thought to produce more tension than those activated at shorter lengths [11]. Due to the timing and velocity of prestretch, muscles stimulated at the peak of stretch actually show a reduction in peak tension when compared to non-stretched beats, emphasizing the role of mechanisms such as the force-velocity relationship.

2.4.2 Work

The timing of prestretch determines the amount of external work done by the muscle (Figure 2.9). Previous studies have concluded that late-activated regions of hearts undergoing ventricular pacing do more external work and also have an increased demand for oxygen [7, 8]. The work calculated in these studies was based on approximations of fiber-stress. In the current study, both fiber-stress and fiber-strain were measured directly, giving more accurate results of both. Stretch timing that mimics prestretch in late-activated regions in-vivo causes increased external work to be performed by the muscle specimen. These results agree with those seen in-vivo [7,

8], and also shows that prestretch may be a large contributor to the work imbalance observed *in-vivo* during regional ventricular pacing.

2.4.3 Myofilament Overlap

Analysis on the effect of myofilament overlap on tension production was performed by observing the effect of stretches peaking near the peak of the calcium transient. It was assumed that stretching to a longer length meant increasing myofilament overlap, due to the starting length of the stretch (an estimated sarcomere length of 2 μm) , and that the magnitude of the stretch (10% strain) would increase overlap by bringing the sarcomere length to roughly 2.2 μm. While it is known that increased myofilament overlap increases tension production in muscle [13], stretches with maximum overlap near the peak of the calcium transient proved not to be the stretches that produced the most peak tension; ultimately meaning that there may be deactivating effects taking place.

2.4.4 Time Varying Stiffness

Time-varying elastance has been shown to play a substantial role in cardiac muscle mechanics, especially in modeling ventricular function. As a muscle contracts, its mechanical stiffness increases, so it is expected that when it is stretched during contraction, the total force of the muscle will increase. As a means of determining the contribution of the change in stiffness, an analysis was performed to determine what forces would have been produced if time-varying stiffness was the only contributor to changes in tension. The red trace in figure 2.13 shows the peak tension values that

would be produced simply due to stretching the tissue while the stiffness is changing, using experimentally measured stiffness values. The results from this analysis show that while time-varying stiffness contributes to the general response of the tissue to prestretch, it cannot completely reproduce the experimental prestretch results. This distinction is important because time-varying stiffness is used to model ventricular contractility [14]. Here we show that time-varying stiffness is not sufficient in explaining the tension response to physiological stretches of isolated cardiac muscle.

When looking at the differences in the peak tensions produced by the prestretch experiments and those that arose through the time-varying stiffness analysis, as in figure 2.13, there is an obvious difference, implying that the time-varying stiffness analysis is not sufficient in reproducing experimental results. As seen in this figure, the time-varying stiffness analysis produces more peak tension for every given timing of prestretch. This implies that in the experiments, there is a deactivating effect that is taking place, preventing peak tensions from reaching those of the time-varying stiffness analysis.

2.4.5 Force-Velocity Effects

The analysis of the prestretch experiments demonstrate that the velocity of shortening and lengthening influence tension development in mouse cardiac papillary muscles. The results also show that time-varying stiffness is not sufficient in explaining the results observed in the prestretch experiments, thus additional mechanisms were investigated in an attempt to explain what time-varying stiffness

could not; one of these mechanisms is the force-velocity relationship. Figure 2.14 examines the difference between the tension predicted by time-varying stiffness and that of the prestretch experiments. Point **c** on the plot occurs during the interval where the prestretches have a maximum shortening velocity near the peak of the calcium transient. This local maximum shows where the time-varying stiffness analysis overestimated the peak tensions the most. This implies that there is a deactivating mechanism that is taking place that is not picked up by the time-varying stiffness. A possible explanation for this first local maximum is that the muscles are undergoing the maximum shortening velocity during the peak of the calcium transient, so they are unable to produce as much force as they would if they were not shortening [15]. The time-varying stiffness analysis cannot account for this effect of shortening velocity; therefore there is a large difference in the peak tensions produced by this analysis and the prestretch experiments.

Point **d** in figure 2.14 also has some implications of the force-velocity relationship. For stretches occurring near this minimum, the time-varying stiffness analysis does not overestimate the peak tensions as much, meaning it produces values closer to that of what is seen experimentally. This could partially be explained by a phenomenon that is increasing the peak tensions in the experiments, but that is not reproduced by the time-varying stiffness analysis. One possible explanation is that the prestretches occurring during this minimum are undergoing maximum lengthening velocity during the peak of the calcium transient. The force-velocity relationship

would imply that this increase in lengthening velocity would increase the peak tensions observed [16].

When looking at individual prestretches, some of the effects that are not reproduced using the time-varying stiffness analysis can also be explained by the force-velocity relationship. The timing of prestretch that produces the least peak tension is compared to the time-varying stiffness prediction for the same timing of stretch in panel A of figure 2.16. Panel B shows the difference between the time-varying stiffness analysis and the experimental tension. The maximum difference in this figure occurs during the maximum velocity of shortening of the prestretch. This maximum difference can partially be explained by the fact that the time-varying stiffness analysis does not include the deactivating effects of shortening.

The force-velocity relationship can also explain some of the differences observed in panel D of figure 2.16. Early in the twitch there is a region where the time-varying stiffness analysis predicts less tension than is observed by the experiments. This interval of the twitch occurs at the same time as the maximum lengthening velocity of the stretch. The time-varying stiffness analysis is not able to reproduce the increase in tension that is produced due an increased lengthening velocity. Later in the twitch, the point of maximum difference between the experiments and the time vary elastance (panel E) can also be explained by the deactivating effects of shortening velocity that are not reproduced by the time-varying stiffness.

2.4.6 Shortening Deactivation

Another mechanism that can explain some of the overestimation of tension that is predicted by the time-varying stiffness analysis is shortening deactivation [17]. This becomes most obvious at point **e** in figure 2.14. This analysis shows that the largest difference between the time-varying stiffness prediction and the experimental results occurs for the prestretches that take place later in the twitch, when the levels of free calcium have decreased. Shortening occurring during lower levels of free calcium has been shown to have a deactivating effect on tension production, as the shortening can cause bound crossbridges to detach, and due to the low levels of calcium bound to troponin-C, crossbridges are not able to rebind to regain previous levels of bound bridges [17]; ultimately preventing tension from reaching magnitudes possible if the shortening had not taken place.

2.4.7 Limitations

While all possible efforts were made to ensure that this study simulated prestretch and analyzed its effects in the best way possible, as with any scientific study, there are some inherent limitations. One limiting factor would be the use of mouse papillary muscles. These muscles generally do not have the ideal characteristic of long parallel fibers that can be seen in cardiac trabeculae, so there are some inherent assumptions that take place with the use of papillary muscles. Due to the attachment of the papillary muscle to the muscle chamber, there is some compliance of the tissue that cannot be avoided, which can lead to problems determining the amount of stretch

actually felt by the muscle. This was dealt with by tracking the strain at the center of the muscle as well as insuring that the muscle was mounted in such a way that there was the least amount of compliance possible. Ultimately papillary muscles were used due to their ability to withstand stretch without damage as well as the possibility of doing similar experiments in genetically modified mice, where papillary muscles are always available for dissection, whereas trabeculae often are not.

2.4.8 Conclusions

In this study, the timing and magnitude of prestretch on mouse papillary muscles were found to influence twitch tension and work. The time-varying stiffness analysis made it clear that while the stiffness changes during contraction have a substantial effect on the twitch tension, it does not fully explain the prestretch experimental results. Further analysis of the results has made it clear that the force-velocity relationship explains much of the results that cannot be explained by the time-varying stiffness analysis. The last major contributor to the prestretch analysis was that shortening deactivation could explain deactivating effect of prestretches occurring late in the twitch when there is little free calcium present. Ultimately, the analysis shows that time-varying stiffness and force-velocity alone cannot explain the effects of prestretch on twitch tension; other mechanisms such as shortening deactivation need to be included. These findings suggest that because mechanisms involving activation and deactivation are needed to explain the results, prestretch must be influencing activation of the myofilaments.

2.5 ACKNOWLEDGEMENTS

Chapter 2, in part, is currently being prepared for submission for publication of the material. Tangney J; Campbell S; McCulloch AD; Omens JH. “Timing and Magnitude of Prestretch Affect Myofilament Activation.” The thesis author was primary investigator and author of this material.

REFERENCES

1. Sweeney, M.O. and F.W. Prinzen, *A new paradigm for physiologic ventricular pacing.* J Am Coll Cardiol, 2006. 47(2): p. 282-8.

2. Coppola, B.A., et al., *Asynchrony of ventricular activation affects magnitude and timing of fiber stretch in late-activated regions of the canine heart.* Am J Physiol Heart Circ Physiol, 2007. 293(1): p. H754-61.

3. Badke FR, B.P., Covell JW, *Effects of ventricular pacing on regional left ventricular performance in the dog.* Am J Physiol Heart Circ Physiol 1980. 238: p. H858–H867.

4. Wyman, B.T., et al., *Effects of single- and biventricular pacing on temporal and spatial dynamics of ventricular contraction.* Am J Physiol Heart Circ Physiol, 2002. 282(1): p. H372-9.

5. Delhaas, T., et al., *Relation between regional electrical activation time and subepicardial fiber strain in the canine left ventricle.* Pflugers Arch, 1993. 423(1-2): p. 78-87.

6. Prinzen, F.W., et al., *Redistribution of myocardial fiber strain and blood flow by asynchronous activation.* Am J Physiol, 1990. 259(2 Pt 2): p. H300-8.

7. Prinzen, F.W., et al., *Mapping of regional myocardial strain and work during ventricular pacing: experimental study using magnetic resonance imaging tagging.* J Am Coll Cardiol, 1999. 33(6): p. 1735-42.

8. Delhaas, T., et al., *Regional fibre stress-fibre strain area as an estimate of regional blood flow and oxygen demand in the canine heart.* J Physiol, 1994. 477 (Pt 3): p. 481-96.

9. van Oosterhout, M.F., et al., *Asynchronous electrical activation induces asymmetrical hypertrophy of the left ventricular wall.* Circulation, 1998. 98(6): p. 588-95.

10. Ford, L.E., A. F. Huxley, and R. M. Simmons, *The relation between stiffness and filament overlap in stimulated frog muscle fibres.* J. Physiol. , 1981(311): p. 219–249.

11. Konhilas, J.P., T.C. Irving, and P.P. de Tombe, *Frank-Starling law of the heart and the cellular mechanisms of length-dependent activation.* Pflugers Arch, 2002. 445(3): p. 305-10.

12. Konhilas, J.P., T.C. Irving, and P.P. de Tombe, *Myofilament calcium sensitivity in skinned rat cardiac trabeculae: role of interfilament spacing.* Circ Res, 2002. 90(1): p. 59-65.

13. Gordon, A.M., A.F. Huxley, and F.J. Julian, *The variation in isometric tension with sarcomere length in vertebrate muscle fibres.* J Physiol, 1966. 184(1): p. 170-92.

14. Suga, H., K. Sagawa, and A.A. Shoukas, *Load independence of the instantaneous pressure-volume ratio of the canine left ventricle and effects of epinephrine and heart rate on the ratio.* Circ Res, 1973. 32(3): p. 314-22.

15. Sonnenblick, E.H., *Force-velocity relations in mammalian heart muscle.* Am J Physiol, 1962. 202: p. 931-9.

16. Morgan, D.L., *New insights into the behavior of muscle during active lengthening.* Biophys J, 1990. 57(2): p. 209-21.

17. Edman, K.A., *Mechanical deactivation induced by active shortening in isolated muscle fibres of the frog.* J Physiol, 1975. 246(1): p. 255-75.

Chapter 3

Novel Role for Vinculin in Myocardial Fiber Mechanics and Heart Failure

ABSTRACT

The membrane-associated cytoskeletal protein vinculin (Vcl) has been shown to play a key structural role in ventricular myocytes that, when disrupted, can lead to dilated cardiomyopathy and heart failure. To elucidate the function of Vcl in sarcomere structure, myocyte mechanics and regional ventricular wall motion. Cardiomyocyte-specific Vcl knockout mice (cVclKO) and littermate control wild type mice were studied with electron microscopy (EM) to quantify sarcomere structure and with *in-vivo* magnetic resonance tagging to measure regional wall strains before the onset of ventricular dysfunction. Cardiac MR tagging revealed significantly decreased systolic strains transverse to the myofiber axis, but no changes in regional systolic fiber strains *in vivo,* consistent with no difference seen in isometric fiber tension development in isolated papillary muscles from heterozygous global Vcl knockout mice. Optical diffraction patterns generated from EM showed that myofilament lattice spacing was significantly greater in unloaded cVclKO *vs.* WT mouse hearts fixed either during cardioplegic arrest or barium contracture. A novel multi-scale

computational model of left ventricular mechanics incorporating the anisotropic effects of crossbridge geometry and lattice mechanics showed that increased transverse systolic stiffness due to increased lattice spacing can explain the altered systolic wall strains associated with Vcl deficiency, prior to overt heart failure. These results suggest that loss of cardiac myocyte Vcl decreases systolic transverse strains *in vivo* by increasing myofilament lattice spacing and stress transverse to the myofibers. This novel mechanism of early mechanical dysfunction may be important in the pathogenesis of heart failure associated with cytoskeletal defects.

3.1 INTRODUCTION

Vinculin (Vcl) is a 117-kDa membrane-associated protein expressed in all cell types. It localizes at both cell-matrix and cell-cell adhesion sites including costameres and intercalated discs in cardiomyocytes [1-3]. Vcl is a key structural component in the formation of costamere protein complexes that link the actin cytoskeleton to integrins on the cell surface of muscle cells [4-7]. Previous studies have shown that suppression of Vcl expression by antisense oligonucleotide treatment of fetal cardiomyocytes causes a disturbance in normal myofibrillar arrangement [8]. Additionally, investigation of heterozygous global Vcl knockout mice (VclKO) showed normal basal cardiac function, abnormal intercalated discs, and a predisposition towards stress-induced cardiomyopathy provoked by aortic constriction [5]. The mouse model utilized in this study has cardiomyocyte-specific reduction of Vcl (cVclKO) and displays abnormal intercalated discs [4]. Half of the cVclKO mice die suddenly, prior to the age of 3 months, and the remainder develop dilated cardiomyopathy (DCM) by 16 weeks of age [4]. The normal expression of Vcl may allow cells to resist stresses that result from mechanical forces on the cell exterior [4], suggesting a structural role in force transmission between the exterior and interior of the myocyte. It has also been suggested that Vcl plays a significant role in mechanotransduction [5]. Therefore Vcl deficiency may contribute to the development of DCM, as was shown in the cVclKO mice. In addition to transducing mechanical signals, Vcl could directly affect mechanical function of the myocardium in a direction-dependent manner owing to its localization at the costamere.

To better understand the role of Vcl in regional cardiac function, the 3D geometric structure of the heart and fiber architecture must be taken into account. Muscle fibers have a distinct helical pattern in the wall of the left ventricle [9]. In addition to fiber orientation, endomysial collagen struts link costameres of adjacent cells together in the transverse direction [10] and may be key to the transmission of forces transverse to the cells. Therefore, weakening of cell-extracellular matrix interactions or redistribution of intracellular forces, as could occur when cells have deficiencies in Vcl, may directly affect mechanics transverse to the myocyte fiber axis.

The goal of this study was to investigate the structural role of Vcl in cardiac myocytes, and to determine the implications for regional mechanics prior to the onset of heart failure in Vcl knockout mice. We hypothesized that altered cytoskeletal structure or force transmission may affect tissue mechanics relative to the muscle fiber structure before the onset of global ventricular dysfunction. Three-dimensional cardiac strains were measured *in vivo* with magnetic resonance imaging (MRI) tagging in control and cVclKO mice at an age of 6-7 weeks before the onset of DCM in cVclKO. There were significant decreases in end-systolic transverse (radial and cross-fiber) strain components with no changes in fiber strains, and no changes in global systolic function.. The structural basis of this dysfunction was examined with ultrastructural quantification of sarcomere lattice spacing, and a multi-scale computational model of ventricular mechanics was used to examine the mechanistic link between measured increases in lattice spacing that occurred with Vcl deletion and the observed alterations in three-dimensional ventricular wall mechanics. These results suggest that

the primary effect of Vcl deficiency on myocyte mechanics is not on axial shortening or force development, but rather on transverse force development by the sarcomeres which in turn compromises regional myocardial function. This finding suggests a novel mechanism for early myocardial mechanical dysfunction that may be important in the pathogenesis of heart failure associated with cytoskeletal defects.

3.2 METHODS

3.2.1 Mice

The cVclKO mice with cardiomyocyte-specific excision of the Vcl gene have been described previously[4]. Cre-negative littermates (WT) with no Vcl excision were used as the controls. The mice used in this study were 6-7 weeks of age from strains that had been maintained in a mixed SV129/Black Swiss background and interbred for at least 10 generations. All protocols were performed according to the National Institute of Health's *Guide for the Care and Use of Laboratory Animals* and approved by the UCSD Animal Subjects Committee.

3.2.2 MRI and Global Function

MRI was performed on a 7T horizontal-bore magnet (Varian, Palo Alto, CA, USA) with an Avance II console (Bruker, Germany). Imaging protocols were based on methods in Chuang *et al.* [11]. An ECG-triggered FLASH sequence was used for cine imaging with the following parameters: TE = 2.3 ms, TR = 6 ms, flip angle = 15°,

slice thickness = 1 mm, NEX = 4, FOV = 2.0 cm, in-plane resolution = $(156\ um)^2$. For MRI tagging, a spatial modulation of magnetization (SPAMM) sequence was used [12] to produce tag lines with a distance of 0.9 mm and width of 0.31 mm (Figure 3.1A). Five short axis images and three longitudinal images were acquired. Cine and SPAMM images were collected at all slice locations. The entire imaging protocol took approximately 1 hour for each mouse.

In the cine images, the myocardium was segmented with a semi-automatic level set algorithm [13] in order to extract the endocardial and epicardial boundaries. A 3D geometric model of the end-diastolic left ventricle (LV) was created (Figure 3.1B) by fitting high-order prolate spheroidal finite element meshes to the endocardial and epicardial points [11]. Cavity and wall volumes were measured from the 3D mesh, and wall mass was calculated by multiplying wall volume with myocardial density (1.05 g/ml).

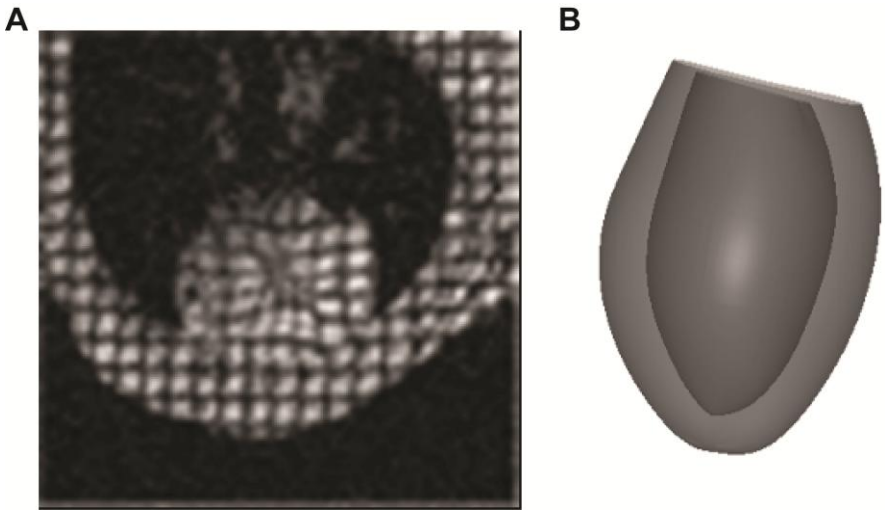

Figure 3.1: (A) MRI tagging of the mouse heart, image at end-systole. (B) 3D geometric model of the mouse LV used for global parameter estimation.

3.2.3 Fiber Strain Analysis

Harmonic phase (HARP) analysis was used to automatically track myocardial material points in the SPAMM images[14]. To calculate 3D Lagrangian strains, a deformable model was created using material point displacements from the HARP analysis. The end-diastolic LV model was deformed to fit material point coordinates at end-systole. End-systolic strains with respect to the cardiac coordinates (circumferential, longitudinal, radial) were calculated at the equator (mid-ventricle) of the LV free wall, at 3 transmural locations (epicardial, midwall and endocardial). Strains were then rotated about the radial axis through the measured fiber angle (see measurements below) to give regional strain in cardiac fiber coordinates (fiber, cross-fiber and radial axes). Details of the implementation of the deformable model can be found in Chuang *et al.* [11].

3.2.4 Isolated Muscle Mechanics

Right ventricular papillary muscles were isolated from adult WT and heterozygous global Vcl KO hearts, and mounted in a cardiac tissue culture chamber as previously described [15]. After preconditioning, the muscles were stimulated at 1 Hz, and stretched from slack length to a passive muscle length with maximum developed systolic force. Peak isometric twitch force was recorded at several passive lengths along with muscle cross-sectional area to determine peak developed fiber stress as a function of passive length.

3.2.5 Histology

After MRI imaging, the mouse hearts were arrested with a hyperkalemic solution and fixed with 10% buffered formalin as described previously [16]. Each heart was cut into three pieces for fiber and sheet angle measurement. Each tissue piece was embedded in optimal cutting temperature compound and cryo-sectioned to produce 10 μm slices. The first block was sectioned through the LV free wall parallel to the epicardial circumferential-longitudinal plane (1-2) for transmural fiber angles (α). A continuous fiber angle distribution through the wall from epicardium to endocardium was calculated by a linear least squares fit of the measured α. The remaining tissue pieces were sectioned parallel to the circumferential radial (1-3) plane or the longitudinal-radial (2-3) surface, for measurement sheet angles (β) as described previously [16].

3.2.6 Sample Preparation for Electron Microscopy (EM)

cVclKO mice (n=6) and littermate controls (n=6) 5-6 weeks of age were euthanized, and the hearts were isolated. The first group of the hearts was arrested at end-diastole by perfusion with a modified St. Thomas' Hospital cardioplegic solution no. 2 [17]; for the second group, barium contracture against zero-load was utilized to simulate end-systole [18, 19] by first perfusing the heart with a modified low-calcium Tyrode solution (0.078 mM $CaCl_2$) for 5 min and then Tyrode solution with 0.078 mM $CaCl_2$ and 2.5 mM $BaCl_2$. Tissue samples were then prepared as described previously with minor modifications [20]. Briefly, the hearts were perfusion fixed with 2% (wt/v) paraformaldehyde and 2.5 % glutaraldehyde. Two-hundred um thick vibratome slices were incubated in 0.8% potassium ferrocyanide and 2% osmium

tetroxide overnight before being stained with 1% uranyl acetate (UA), dehydrated in ethanol, and embedded in Durcupan ACM resin.

3.2.7 Myofilament Image Analysis

150-200 nm thickness sections for EM were stained with 1% UA and Sato lead. Sets of images were obtained on a FEI Titan electron microscope operated at 300 kV. The tilt angle of the stage was adjusted manually such that the tissue was oriented for proper sectioning relative to the local fiber direction as quantified previously in the mouse [16]. In order to quantify myofibril interfilament lattice spacing, images were recorded at 37,000x or 47,000x magnification by a Gatan 4K x 4K Ultrascan 4000 CCD camera with myocytes oriented approximately normal to the plane of the image. Sarcomere length (SL) images were recorded at 3,800x or 5,000x magnification by the same camera in the plane of the cell long axis. All images were processed within ImageJ. A square region of interest (ROI, 4096 by 4096 pixels) was selected at the A bands with both thick and thin filaments visible, and transformed into the spatial frequency domain by fast Fourier transformation (FFT). The distance to the first- and second-order diffraction patterns of the lattice images were converted into median inter-thick filament spacing and lattice spacing (thick to thin filament spacing) respectively across the region, while the first-order diffraction pattern from long axis sarcomere images was utilized to determine a median sarcomere length[21]. A minimum of 12 ROIs was used in each animal for lattice spacing, and 18 ROIs from each for sarcomere length.

3.2.8 Crossbridge Mechanics Model

A micromechanical model of three-dimensional myofilament mechanics was used to derive transverse systolic sarcomere stiffness as a function of crossbridge stiffness based on crossbridge geometry and actomyosin lattice spacing (Figure 3.2). Following the analysis by Schoenberg [22], the S2 segment of the crossbridge was modeled as a spring with a freely jointed hinge at the origination site on the thick filament backbone. An S2 origin azimuthal position of 90^o was used, with an actin-binding site azimuthal position of 90^o, an axial tilt angle at the attachment site (α, Figure 3.2A, 3.2B) of 45^o [23, 24]. Since the S2 origin site was modeled as a freely rotating pivot point, the angle between the thick filament and the S2 region of myosin (θ in Figure 3.2E,F) was constrained by the other angles and geometries used, and therefore varies as a function of lattice spacing (Δ). These assumptions are sufficient to allow the crossbridge force F_{S2} to be resolved into longitudinal (fiber) and crossfiber (transverse) force components, F_{ff} and F_{tt}, respectively as originally derived by Schoenberg [22]. Note that an increase in lattice spacing increases the crossbridge tension by increasing crossbridge strain and increases the ratio of F_{tt} to F_{ff} by increasing □ (Figure 3.2A, 3.2B). Using this approach to incrementally increase the lattice spacing, the resulting changes to F_{tt} and F_{ff} can be used to calculate the ratio of transverse to fiber crossbridge stiffnesses (K):

$$\frac{K_{tt}}{K_{ff}} = \frac{l_{S2} - \hat{l}_{S2}cos^2\theta}{l_{S2} - \hat{l}_{S2}sin^2\theta} \quad [3.1]$$

where l_{S2} and $\hat{l}_{S2}$are the instantaneous and resting lengths of the S2 segment of myosin, respectively.

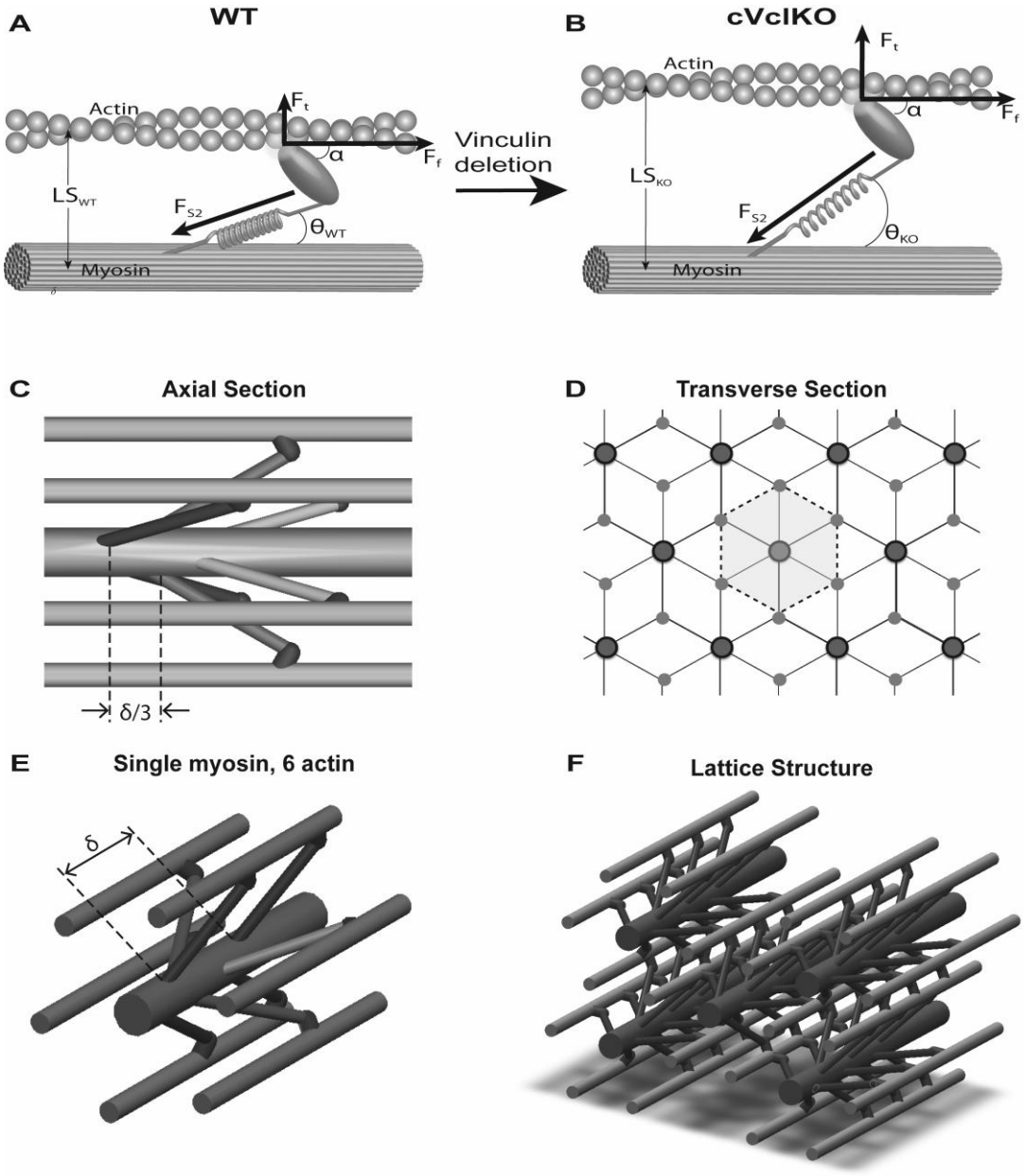

Figure 3.2: Schematic depiction of a micromechanical model for sarcomere lattice spacing and cross-bridge architecture. The individual cross-bridge model consisting of a myosin stalk based on the geometry by Schoenberg [22] is shown in panel A. As the lattice spacing (LS) increases with Vcl deletion (transition from panels (A) to (B)), binding angles (θ) change and F_{S2} increases (modeled as a spring). The result is an increase in the transverse force, but little change in the fiber force. (F_t = transverse force, F_f = fiber force, F_{S2} = force along S2 segment). The unit cell of the lattice structure used for analysis in the two directions, axial (C) and transverse (D), which is marked with a dotted outline. Panel E shows a single myosin thick filament surrounded by six actin filaments, and Panel F shows the overall lattice structure. Details of the myofilament lattice mechanics model can be found in the Supplement.

3.2.9 Myofilament Lattice Mechanics Model

To compute macroscopic three-dimensional transverse:fiber stiffness ratios, we consider the myofilament lattice geometry in planes transverse and parallel to the myofilaments (Figures 2C, 2D) when all crossbridges are attached in the strongly bound state. By deriving the strain energy associated with equibiaxial transverse strain of the lattice and uniaxial fiber strain of the sarcomeres (see Online Supplement), we obtain the following expression for the ratio of the transverse lattice stress (σ_{tt}) to the fiber lattice stress (σ_{ff}):

$$\frac{\sigma_{tt}}{\sigma_{ff}} = \frac{1}{2}\left(\frac{\Delta}{\delta}\right)\frac{K_{tt}}{K_{ff}} \qquad [3.2]$$

where δ is the distance along the thick filament between consecutive cross-bridge pairs in the same plane (Figure 3.2E) and also represents the length of a hexagonal unit element, with six crossbridges and a radius equal to the actomyosin lattice spacing (Δ) (Figure 3.2C, 3.2D).

To use these expressions in a continuum constitutive model of systolic myocardial stress, the current SL is calculated from the macroscopic fiber strain using the unloaded reference sarcomere length (SL_0) that was measured for each genotype from the electron micrographs of unloaded cardioplegia-arrested hearts. The time-varying myofilament lattice spacing was computed from the sarcomere length (S) using the assumption that sarcomere volume (V_s) remains constant during the cardiac cycle, i.e. $S \times \Delta^2 = V_S$. The volume constant V_S for each genotype was based directly on EM measurements in the diastolic and systolic arrested preparations, which also

supported the assumption that the lattice deformed isotropically during contraction (i.e. even though the ventricle thickened radially and shortened transverse to the fibers in the plane of the wall, the interfilament distances remained independent of orientation in the plane transverse to the filaments). V_S, derived from the electron micrographic measurements, was scaled up by 20% in both genotypes to account for the previously reported effects of lattice shrinkage due to dehydration and fixation, which only affects lattice spacing and not the SL [25].

In summary, by considering the mechanical equilibrium of the crossbridge and myofilament lattice in three dimensions, we derived a micromechanical model for dynamic systolic stiffnesses in the fiber and transverse directions as a function of sarcomere length, lattice spacing and time. A kinematic model in turn enables the SL and lattice spacing to be determined from macroscopic fiber strains. The only parameters in this analysis that were varied between genotypes in this analysis were measured directly from the electron micrographs. This microstructural model was included in a finite element model of ventricular mechanics, described below, to test whether measured alterations in sarcomere geometry were sufficient to explain observed mechanics *in vivo* in young WT and VclKO mice.

3.2.10 Ventriclar Mechanics Model

To investigate the effect of sarcomere ultrastructural alterations due to Vcl deficiency on systolic wall mechanics, a finite element model of a mouse LV was created using a thick truncated ellipsoid of revolution [26]. The focal length of the

prolate spheroid was 3.75 mm. At zero pressure, the cavity volume of the mesh was 30 µl. The myocardium was modeled as a slightly compressible, transversely isotropic material with respect to the fiber and transverse-fiber directions [27]. Average transmural fiber angle distributions measured in this study were used in the model. The unloaded geometry was passively inflated to an end-diastolic pressure of 10 mmHg.

Systolic material properties were obtained by adding active fiber and transverse stresses as functions of SL and time computed using the microstructural model described above. Resting myocardial material properties were modeled for both genotypes using a transversely isotropic exponential strain energy function[28] with parameters as given in the Online supplement. Length- and time-dependent contractile activation during systole was modeled using the Guccione[42] model with parameters that were the same for both genotypes as given in the Online Supplement. The LV was simulated to contract against a three-element Windkessel model [29] with an initial aortic pressure of 80 mmHg. Left ventricular and aortic pressures were used to determine closure of the aortic valve and the end-systolic time point. Thus this 3D functional model of the LV incorporated structural changes at the sarcomere level and was able to compute regional systolic strains in both WT and CVclKO models that could be compared with the MRI-derived measurements.

3.2.11 Statistics

All measurements are presented as mean ± SD. End-systolic strains, sarcomere geometry measurements between cVclKO and WT mice, and fiber were

compared by two-way repeated measures ANOVA. P-values < 0.05 were considered significant. To identify the effects of genotype on LS independent of differences in SL, the relationship was analyzed using analysis of covariance (ANCOVA) in which the regressor was $1/\sqrt{SL}$ based on the assumption of sarcomere volume conservation. To test the statistical significance of the results predicted by the model, z-scores were assigned to all the model strain results based on the experimental means and standard deviations.

3.3 RESULTS

3.3.1 Global Geometry and Function

From the geometric models based on the cine images of the myocardium, end-diastolic volume (EDV), end-systolic volume (ESV), ejection fraction (EF), and left ventricular mass index (LVMI) were measured. EDV (48±12 vs. 50±11 μl) and ESV (20±8 vs. 25±6 μl) were slightly larger in cVclKO, but not significantly different. There were also no significant differences in EF (58±9 vs. 50±4 %) and LVMI (4.2±0.9 vs. 4.1±0.7 mg/g) between cVclKO and WT mice, respectively. cVclKO lung and liver weights were within the normal range (data not shown). Peak systolic fiber stress was not different at any passive muscle length as determined from isolated papillary muscle studies (data not shown).

3.3.2 Fiber and Sheet Angles

Transmural fiber angles at the equator of the LV free wall were measured from histology. Figure 3.3 shows the linear distribution of fiber angles (α) for cVclKO and WT hearts. There was no significant difference in α between cVclKO and WT hearts at this location. The fiber angles varied linearly from negative values at the epicardium to positive values at the endocardium as expected. Sheet angles were on average negative throughout the wall, varying from -42º to -65º at the mid-ventricle, similar to previously reported values [16]. There were no significant differences in sheet angles between cVclKO and WT hearts.

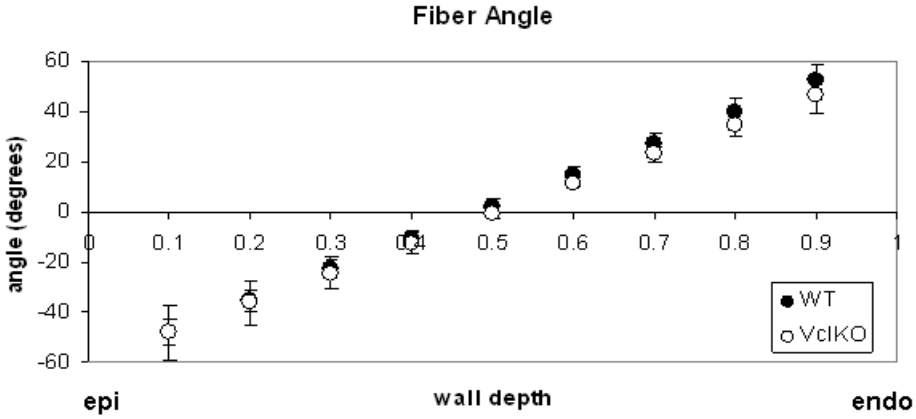

Figure 3.3: Measured transmural fiber angle distributions in WT and cVclKO hearts, shown at normalized depths between epicardium (epi) to endocardium (endo). There were no statistical differences between the 2 groups.

3.3.3 Regional Strains

Regional midventricular strain tensors computed from the HARP analysis at three transmural locations and resolved with respect to local fiber coordinates (f = fiber, c = cross-fiber, r = radial) using the measured fiber angles are shown in Figure 3.4 at end-systole referred to an undeformed reference state at end-diastole. In WT mice, systolic fiber strain (E_{ff}) was negative (shortening) and uniform across the wall. Cross-fiber strain (E_{cc}) was also negative as expected and radial strain (E_{rr}) was positive consistent with systolic wall thickening, and both of these components were largest at the subendocardium and smallest at the epicardium, as seen previously in the mouse [11] and other species [30]. In cVclKO hearts, two way ANOVA anlaysis showed that E_{ff} was not different from WT, however the transverse components of strain (E_{cc} and E_{rr}) showed significant differences of interaction ($p<0.05$), implying a difference in the way the strain vary transmurally. There was also a significant difference ($p<0.05$) between genotypes regardless of transmural location for E_{rr}. All of the shear strains were relatively small in magnitude, but a genotype difference ($p<0.05$) was observed for both E_{fc} and E_{cr}. Overall, Vcl deficiency significantly reduced myocardial systolic strains transverse to the myocytes but had no effect on systolic fiber shortening.

Table 3.1: Two way ANOVA results performed to show the difference between WT and cVclKO strains based on location through the wall and genotype. Statistically significant values ($p<0.05$) are shown with a thick box around the cell.

		Eff	Ecc	Err	Efc	Efr	Ecr
Two way ANOVA	Genotype (p-value)	0.799	0.618	***0.000***	***0.002***	0.879	***0.015***
	Wall Location (p-value)	0.210	***0.000***	0.976	0.053	0.965	0.629
	Interaction (p-value)	0.638	***0.010***	***0.001***	0.548	0.990	0.871

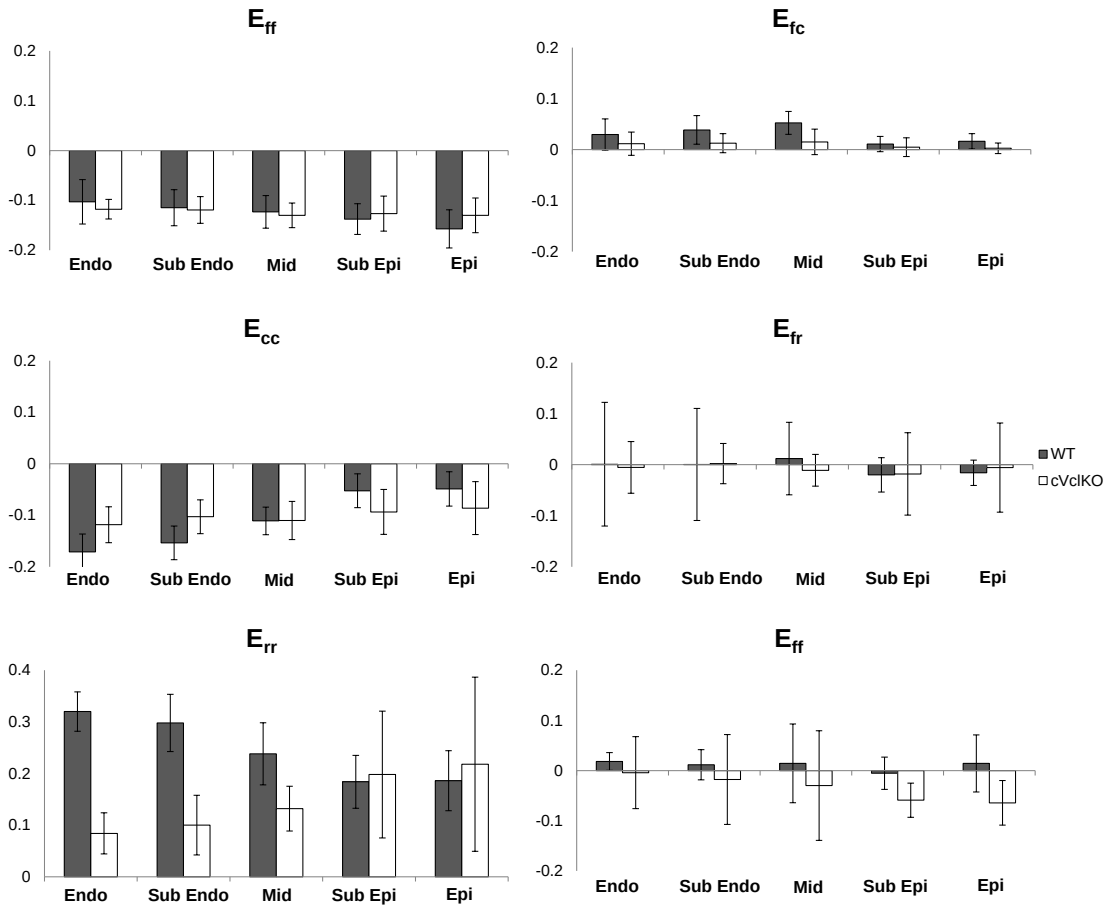

Figure 3.4: Regional end-systolic fiber strains found from MRI imaging and 3D model analysis at 5 transmural locations. 6 strain components are referenced to the local fiber coordinate system (f=fiber, c=cross-fiber, r=radial axes). Values and gradients for WT are as expected, and statistical comparison between WT and cVclKO shows decreases in strain magnitude predominately for the transverse normal strains (E_{rr} and E_{cc}).

3.3.4 Sarcomere Geometry

Myofilament lattice dimensions measured from optical diffraction patterns computed from transmission electron micrographs (Figure 3.5A) are shown in Table 3.2. Lattice spacing obtained from the second order diffraction distance and inter-thick filament spacing from the first-order diffraction pattern were both larger for VclKO mice than WT animals. Their mean ratio (1.70) was within 1.9% of $\sqrt{3}$, the ratio as derived for a hexagonal lattice. Sarcomere lengths were also slightly lower ($p=0.051$) in the KO mice, so to compare lattice dimensions independent of SL we plotted LS *vs.* $1/\sqrt{SL}$. By ANCOVA there was a significant effect of genotype ($p<0.05$) and a signification effect of contractile state ($p<0.05$). The slope of this relation is the sarcomere volume constant V_S which is also shown for each specimen in Table 3.2 ($p=0.098$).

Table 3.2: Sarcomere length (SL), myosin-myosin lattice spacing (M-M LS), and actin-myosin lattice spacing (A-M LS) measurements for cVclKO (n=3) and WT hearts arrested at end-diastole (n=3) with calcium-free Tyrode solution, and hearts contracted with barium against zero load (n=3). The myosin-myosin volume (M-M Vol) was calculated using M-M LS and SL with the assumptions of constant volume and cylindrical shape. The ANOVA results show that there is a significant genotype difference as well as a significance due to contractile state for both the M-M LS and the A-M LS.

		SL (um)	M-M LS (nm)	A-M LS (nm)	M-M Vol (μm^3)
Relaxed Unloaded Hearts	VclKO	1.77	32.98	19.45	1.92
		1.69	35.00	20.44	2.07
		1.76	32.44	19.15	1.86
	Avg ± std	**1.74 ± 0.04**	**33.47 ± 1.35**	**19.67 ± 0.68**	**1.94 ± 0.11**
	WT	1.90	30.05	17.66	1.71
		1.87	31.34	19.05	1.84
		2.19	31.08	19.56	2.12
	Avg ± std	**1.99 ± 0.18**	**30.83 ± 0.68**	**18.76 ± 0.98**	**1.89 ± 0.21**
Ba-Contracted Unloaded Hearts	VclKO	1.39	39.94	21.89	2.22
		1.53	37.74	21.01	2.17
		1.37	35.16	20.99	1.70
	Avg ± std	**1.43 ± 0.08**	**37.61 ± 2.39**	**21.30 ± 0.52**	**2.03 ± 0.29**
	WT	1.42	31.79	18.70	1.43
		1.43	34.70	19.93	1.72
		1.64	32.22	19.82	1.71
	Avg ± std	**1.50 ± 0.13**	**32.90 ± 1.57**	**19.49 ± 0.68**	**1.62 ± 0.16**
		SL	**M-M LS**	**A-M LS**	**M-M Vol**
Two way ANOVA	Genotype (p-value)	0.051	***0.0043***	***0.012***	0.098
	State (p-value)	***0.0004***	***0.01***	***0.024***	0.29
	Interaction (p-value)	0.22	0.3	0.32	0.098

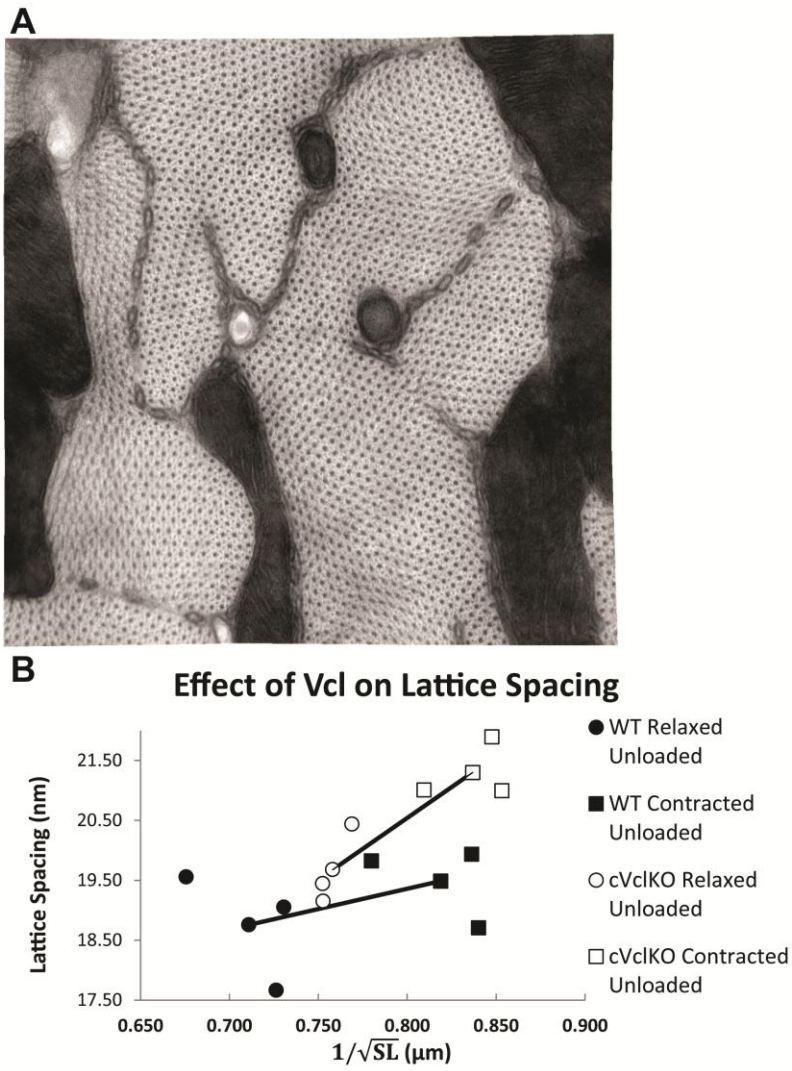

Figure 3.5: Lattice spacing image analysis. (A) Representative EM image montage at x47,000 magnification showing myofilament cross-sections. The pixel size is 0.19 nm, and the image size is 2.3µm x 2.3 µm. (B) Effect of Vcl deletion on actin-myosin filament spacing in mouse hearts arrested at end-diastolic (smaller $1/\sqrt{SL}$) and barium-contracted states (larger $1/\sqrt{SL}$). Assuming constant volume, LS varies with $1/\sqrt{SL}$. Line connects average points.

3.3.5 Ventricular Strains from Model Analysis

Online Supplemental Table A1 summarizes all of the myofilament lattice mechanics as well as the finite element model parameters; the only parameters that were different between the models of the WT and cVClKO mice were those derived from the electron micrographs: unloaded reference SL (1.88 μm WT and 1.74 μm cVclKO), unloaded systolic SL (1.50 μm WT and 1.43 μm cVclKO) and volume constant V_S from which lattice spacing was computed (1620 $nm^2/\mu m$ WT and 2030 $nm^2/\mu m$ cVclKO). End-systolic strain components in fiber/cross-fiber coordinates referred to end-diastole are shown in Figure 3.6 for WT and cVclKO models and compared with experimental results from the MRI tagging experiments. Fiber strains computed with the models were similar to experimental measurements and did not differ significantly between WT and KO cases (using experimental measured variances for comparing the model results statistically). The radial strain decreased substantially with the increased lattice spacing, and the cross-fiber strain decreased at the endocardium and midwall, but increased slightly at the epicardium with an increase in lattice spacing due to loss of Vcl, similar to the trend that was observed experimentally.

All z-scores showed that model results were within two standard deviations of the mean experimental values ($z<2$). In addition to the systolic strains, the model predicted an EF of 49% for WT and 39% for cVclKO. Statistical analysis of predicted values using the variance of the experimental EF showed moderate significant

difference ($p = 0.045$), while experimental values for EF were not statistically different ($p = 0.08$).

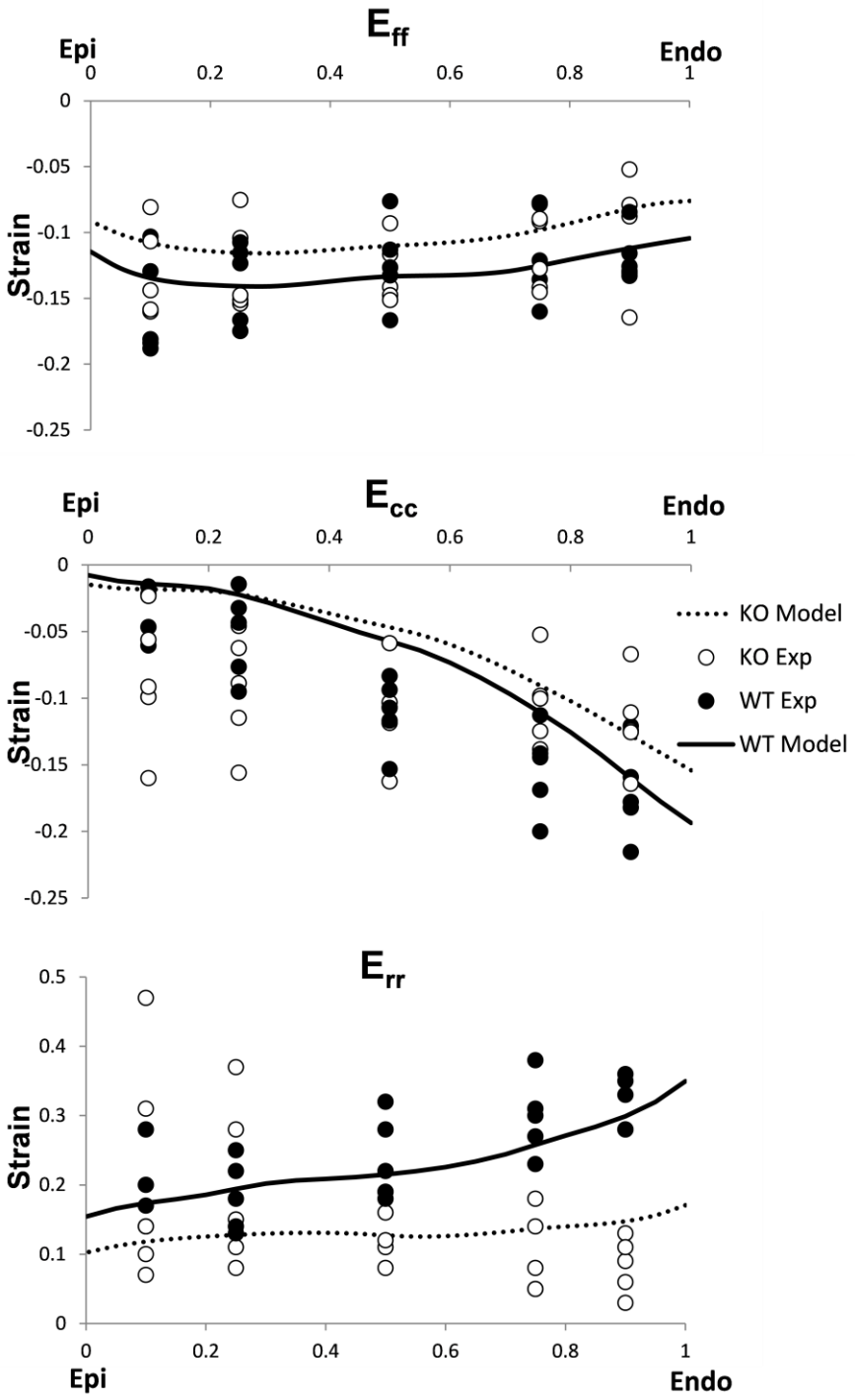

Figure 3.6: Comparison of fiber (E_{ff}), cross-fiber (E_{cc}), and radial (E_{rr}) systolic strains predicted by the finite element model to those measured experimentally using MRI tagging. Gradients and magnitudes are mostly similar indicating general agreement with model and experiment.

3.4 DISCUSSION

In this study, we examined the effect of Vcl deletion and hence Vcl deficiency on sarcomeric structure, and the possible mechanistic link between sarcomere function and regional fiber mechanics in the intact mouse heart. cVclKO mice were studied at a young age before the onset of cardiac dysfunction in order to isolate the effects of the protein deficiency without secondary effects from overt heart disease. The experimental results combined with the mechanistic model analysis indeed indicate that Vcl deficiency can have a direction-dependent effect on regional wall mechanics that can be explained by altered transverse stiffness and force development at the crossbridge level.

Global function at 6-7 weeks of age in this mouse model, as shown by EDV and EF calculated from the geometries in the WT mice were near the ranges reported in literature [31-33]. Slight differences may be attributed to background strain, age, and anesthesia levels. On average, cVclKO hearts were slightly larger than WT hearts and EF was minimally lower, but there were no significant differences detected in any of the global parameters. Therefore, loss of Vcl did not significantly affect global systolic function or geometry in the animals studied here.

The 3D end-systolic strains in the WT free wall agree well with previously published mouse data in terms of magnitude and sign [34, 35]. Our WT data shows that E_{rr} is positive, indicating systolic wall thickening, and it is generally larger at the endocardium than the epicardium. In-plane strains were negative as expected, and

torsional strain was also as expected. Fiber architecture in the cVclKO hearts was not different from that found in control hearts, and was consistent with previously published mouse data [16]. Transforming strains into fiber coordinates provides insight into fiber and transverse-fiber function. The sign and magnitude of systolic fiber strain components in WT mice were similar to values measured in large animals such as the dog [30, 36]. In cVclKO mouse hearts, end-systolic E_{ff} strain was not significantly different from WT hearts, but E_{rr} and E_{cc} were decreased at several locations. This change in transverse function led to the hypothesis that sarcomere lattice spacing is altered by Vcl deficiency, and hence further histological examination.

The reduction in normal Vcl expression was hypothesized to alter the lattice spacing by changing the equilibrium of stresses in the cytoskeleton. On average, the myofilament lattice spacing in cVclKO hearts was larger than the WT hearts at both contraction states suggesting the presence of a cytoskeletal pre-stress acting tangentially to the Z-disk that is partially released when Vcl is deficient. Sarcomeric structure has been shown to be closely linked to mechanical function; shrinkage or expansion of the lattice beyond the equilibrium dimensions causes changes in physiological performance, which is exemplified by altered calcium sensitivity, isometric force, and fiber stiffness [25]. The exact mechanism by which costamere-associated proteins alter the sarcomere lattice spacing needs further investigation.

Previously published x-ray diffraction results for vertebrate heart muscle [37] yielded a lattice spacing of 37 nm at a SL of 2.2 μm, which corresponds to a center-to-center distance between myosin filaments of 42 nm. Lattice spacing measurements

from WT mice were consistent with these values after accounting for lattice shrinkage due to EM sample preparation methods [25]. The slight differences may be attributed to the strain used for this study or the transmural measurement location. The accuracy of the structural measurements is dependent upon the two groups being at the same state of contraction. Because this was likely not the case, the lattice spacing of each mouse was normalized to its sarcomere length to eliminate the variations in SL due to differences in the state of fixation. The normalized lattice spacing of the ED hearts were significantly higher ($P<0.05$) in the cVclKO hearts as compared to the control hearts; a similar trend was observed in the barium-contracted hearts, but no significant differences were observed.

The accuracy of the EM measurements is limited by the different transmural locations utilized for the lattice spacing and SL measurements. The measurements would ideally be taken at the same transmural location due to the previously reported transmural variability of sarcomere length [38]. At this time, it is unknown whether a similar trend exists in the mice used for this study. Regardless, the lattice spacing and sarcomere length measurements were not measured at the exact same transmural location due to limitations in the tissue dimensions and technical issues with the EM.

The micromechanical model used here assumed that the increased lattice spacing in the cVclKO hearts increases the crossbridge angle, which would increase the transverse sarcomere stiffness and generated transverse force assuming no change in the location of the actin binding site. Because the location of the actin binding site was assumed to be the same between the two genotypes, the increased crossbridge

angle caused an increase in strain in the S2 segment of the myosin head. Due to the fact that the S2 segment was modeled as a spring, the increased strain resulted in an increased force in this segment (as seen in Figure 3.2). As a result, the crossbridge active stress increased in the transverse direction but remained approximately constant along the fiber direction. This gave rise to a transverse stress on the lower end of the range recently determined by more complex models of the crossbridge [39]. This analysis implies that a more sophisticated model could show an even more dramatic increase in the transverse component of force with an increase in lattice spacing, improving the agreement of model simulations and experiments.

The crossbridge mechanics analysis was performed using angles and geometric lengths that were either previously referenced in literature or measured for this study. The values that were changed between the WT and cVclKO simulations were differences that were directly measured experimentally. No free or adjustable parameters were used to model or enhance the effects of Vcl deficiency in the active contraction simulations. The two angles in which only a range of angles were available in literature were the S2 origin azimuthal position (θ) and the actin binding site azimuthal position (ϕ)[22]. The effects of these angles were measured by altering their values through the reported range and observing the results. Within this range, the effect of these angles on the difference in strain between cVclKO and WT proved not to be statistically significant. Therefore, the angles chosen do not play a significant role in the outcome of the study.

Active contraction simulations of the cVclKO model revealed systolic strain trends similar to those observed experimentally. The fiber strains of the baseline control simulation exhibit a transmural gradient, which is not consistent with the uniform transmural variation previously reported [40, 41] and the MRI tagging results. The radial and cross-fiber strains have been previously shown to have substantial transmural gradients and are largest at the endocardium [40, 41], both of which are exhibited in the baseline simulation.

The altered sarcomere geometry of the cVclKO mice results in decreased radial strain as predicted in the stress analysis of the crossbridge. However, the simulation fiber strain remains approximately unchanged; this result is consistent with the experimental outcomes and preliminary studies in isolated papillary muscles of heterozygous global cVclKO mice that show no difference in isometric fiber tension development at the studied age. The cross-fiber strain is decreased in the cVclKO model throughout the wall, which agrees very closely to experiments at the endocardium, but the agreement differs slightly at the midwall and epicardium. This disagreement is most likely due to the high levels of variability in the measured cross-fiber strains. Additionally, it was determined that the increase in transverse active stress decreases the amount of wall thickening at end-systole when Vcl function is altered, which is consistent with experimental observations. The magnitudes of the genotypic changes in the simulation were less than the measured values, suggesting that the measured changes in sarcomeric structure may not be the only mechanism responsible for the altered ventricular function associated with Vcl deletion.

There are several possible sources of error associated with the active contraction simulations. First, the fiber angles were only measured at the equator because of the difficulty associated with measuring them; these angles were then incorporated throughout the mesh. Second, no transmural SL gradient was included in the model because no data has been collected to show that it exists in the mouse model being studied. However, if it was determined that this gradient did exist, it would affect the accuracy of the SL measurements as previously described, and its absence would alter the simulation results. Finally, the simplifying assumptions of the model (i.e. ignoring the higher order sheet structure, modeling the myocardium as a transversely isotropic material, no fiber dispersion, etc.) together with the simple axisymmetric geometry of the mesh create a model that may not be capable of accurately depicting all of the mechanistic subtleties associated with Vcl deletion.

The results of the present study are an important step in understanding the mechanistic link between cellular structural alterations and ventricular dysfunction associated with Vcl deletion and Vcl protein deficiency prior to the onset of DCM remodeling. MRI tagging studies defined a specific mechanical defect in ventricular wall function that precedes any decrease in fiber shortening or global chamber function. This defect in mechanical function can be explained by a specific and measurable direction-dependent ultrastructural change at the sarcomere level due to loss of costamere-associated Vcl. This is a novel mechanism for contractile dysfunction and our data likely are applicable to explain how other proteins in the

costamere and dystrophin-glycoprotein complex might lead to human cardiomyopathies.

3.5 Acknowledgements

Chapter 3, in full, is beign prepared for submission for publication of the material. Chuang J and Tangney J; Janssen M, Krishnamurthy A; Liao P, Hoshijima M; Zemljic-Harpf A; Ross R; Frank L; McCulloch AD; Omens JH. “Novel Role for Vinculin in Myocardial Fiber Mechanics and Heart Failure.” The thesis author was a primary investigator and co-first author of this material.

REFERENCES

1. Rudiger M, Korneeva N, Schwienbacher C, Weiss EE, Jockusch BM. Differential actin organization by vinculin isoforms: implications for cell type-specific microfilament anchorage. *FEBS Lett.* 1998;431:49-54.

2. Schlaepfer DD, Hunter T. Signal transduction from the extracellular matrix - a role for the focal adhesion protein-tyrosine kinase FAK. *Cell Struct Funct.* 1996;21:445-450.

3. Hildebrand JD, Schaller MD, Parsons JT. Identification of sequences required for the efficient localization of the focal adhesion kinase, pp125FAK, to cellular focal adhesions. *J Cell Biol.* 1993;123:993-1005.

4. Zemljic-Harpf AE, Miller JC, Henderson SA, Wright AT, Manso AM, Elshrif L, Dalton ND, Thor AK, Perkins GA, McCulloch AD, Ross RS. Cardiac-myocyte-specific excision of the vinculin gene disrupts cellular junctions, causing sudden death or dilated cardiomyopathy. *Mol Cell Biol.* 2007;27(21):7522-7537.

5. Zemljic-Harpf AE, Ponrartana S, Avalos RT, Jordan MC, Roos KP, Dalton ND, Phan VQ, Adamson ED, Ross RS. Heterozygous inactivation of the vinculin gene predisposes to stress-induced cardiomyopathy. *Ame J Pathol.* 2004;165(3):1033-1044.

6. Palmer SM, Playford MP, Craig SW, Schaller MD, Campbell SL. Lipid binding to the tail domain of vinculin: Specificity and the role of the N and C termini. *J Biol Chem.* 2009;284(11):7223-7231.

7. Goldmann WH, Galneder R, Ludwig M, Xu W, Adamson ED, Wang N, Ezzell RM. Differences in elasticity of vinculin-deficient F9 cells measured by magnetometry and atomic force microscopy. *Exp Cell Res.* 1998;239(2):235-242.

8. Shiraishi I, Simpson DG, Carver W, Price R, Hirozane T, Terracio L, Borg TK. Vinculin is an essential component for normal myofibrillar arrangement in fetal mouse cardiac myocytes. *J Mol Cell Cardiol.* 1997;29:2041-2052.

9. LeGrice IJ, Smaill BH, Chai LZ, Edgar SG, Gavin JB, Hunter PJ. Laminar structure of the heart: ventricular myocyte arrangement and connective tissue architecture in the dog. *Am J Physiol Heart Circ Physiol.* 1995;269:H571-H582.

10. Samarel AM. Costomeres, focal adhesions, and cardiomyocyte mechanotransduction. *Am J Physiol Heart Circ Physiol.* 2005;289:H2291-H2301.

11. Chuang JS, Zemljic-Harpf A, Ross RS, Frank LR, McCulloch AD, Omens JH. Determination of three-dimensional ventricular strain distributions in gene-targeted mice using tagged MRI. *Magn Reson Med.* 2010;64(5):1281-1288.

12. Axel L, Dougherty L. MR imaging of motion with spatial modulation of magnetization. *Radiology.* 1989;171:841-845.

13. Yushkevich PA, Piven J, Hazlett HC, Smith RG, Ho S, Gee JC, Gerig G. User-guided 3D active contour segmentation of anatomical structures: Significantly improved efficiency and reliability. *Neuroimage.* 2006;31:1116-1128.

14. Osman NF, Kerwin WS, McVeigh ERP, J L. Cardiac motion tracking using CINE harmonic phase (HARP) magnetic resonance imaging. *Magn Reson Med.* 1999;42:1048-1060.

15. Raskin AM, Hoshijima M, Swanson E, McCulloch AD, Omens JH. Hypertrophic expression induced by chronic stretch of excised mouse heart muscle. *Mol Cell Biomech.* 2009;6(3):145-159.

16. Omens JH, Usyk TP, Li Z, McCulloch AD. Muscle LIM protein deficiency leads to alterations in passive ventricular mechanics. *Am J Physiol Heart Circ Physiol* 2002;282:H680-H687.

17. Jynge P, Hearse DJ, Feuvray D, Mahalu W, Cankovic-Darracott S, O'Brien K, Braimbridge MV. The St. Thomas' hospital cardioplegic solution: a characterization in two species. *Scand J Thorac Cardiovasc Surg Suppl.* 1981;30:1-28.

18. Chen J, Liu W, Zhang H, Lacy L, Yang X, Song S, Wickline SA, Yu X. Regional ventricular wall thickening reflects changes in cardiac fiber and sheet structure during contraction: quantification with diffusion tensor MRI. *Am J Physiol Heart Circ Physiol.* 2005;289:H1898-H1907.

19. Munch DF, Comer HT, Downey JM. Barium contracture: a model for systole. *Am J Physiol Heart Circ Physiol.* 1980;239:H438-H442.

20. Hayashi T, Martone ME, Yu Z, Thor A, Doi M, Holst MJ, Ellisman MH, Hoshijima M. Three-dimensional electron microscopy reveals new details of

membrane systems for Ca2+ signaling in the heart. *J Cell Sci.* 2009;122:1005-1013.

21. Suzuki S, Tsuchiya T, Oshimi Y, Takei T, Sugi H. Electron microscopic studies on the stretch-induced disordering of the myofilament lattice in tetanized frog skeletal muscle fibers. *J Electron Microsc (Tokyo).* 1989;38:60-63.

22. Schoenberg M. Geometrical factors influencing muscle force development: I. The effect of filament spacing upon axial forces. *Biophys J.* 1980;30:51-68.

23. Julian FJ, Moss RL, Sollins MR. The mechanism for vertebrate striated muscle contraction. *Circ Res.* 1978;42:2-14.

24. Rayment I, Holden HM, Whittaker M, Yohn CB, Lorenz M, Holmes KC, Milligan RA. Structure of the actin-myosin complex and its implications for muscle contraction. *Science.* 1993;261:58-65.

25. Millman BM. The filament lattice of striated muscle. *Physiol Rev.* 1998;78:359-391.

26. Costandi PN, Frank LR, McCulloch AD, Omens JH. Role of diastolic properties in the transition to failure in a mouse model of the cardiac dialation. *Am J Physiol Heart Circ Physiol.* 2006;291:H2971-H2979.

27. Doll S, Schweizerhof K. On the development of volumetric strain energy functions. *J Appl Mech.* 2000;67:17-21.

28. Guccione JM, McCulloch AD, Waldman LK. Passive material properties of intact ventricular myocardium determined from a cylindrical model. *J Biomech Eng.* 1991;113:42-55.

29. Kerckhoffs RC, Neal ML, Gu Q, Bassingthwaighte JB, Omens JH, McCulloch AD. Coupling of a 3D finite element model of cardiac ventricular mechanics to lumped systems models of the systemic and pulmonic circulation. *Ann Biomed Eng.* 2007;35(1):1-18.

30. Ashikaga H, Omens JH, Ingels NB, Jr, Covell JW. Transmural mechanics at left ventricular epicardial pacing site. *Am J Physiol Heart Circ Physiol.* 2004;286:H2401-H2407.

31. Croisille P, Rotaru C, Janier M, Hiba B. Gender and strain variations in left ventricular cardiac function and mass determined with magnetic resonance imaging at 7 tesla in adult mice. *Invest Radiol.* 2007;42:1-7.

32. Stegger L, Heijman E, Schafers KP, Nicolay K, Schafers MA, Strijkers GJ. Quantification of left ventricular volumes and ejection fraction in mice using PET, compared with MRI. *J Nucl Med* 2009;50:132-138.

33. Zhong J, Liu W, Yu X. Transmural myocardial strain in mouse: quantification of high-resolution MR tagging using harmonic phase (HARP) analysis. *Magn Reson Med.* 2009;61:1368-1373.

34. Zhong J, Liu W, Yu X. Characterization of three-dimensional myocardial deformation in the mouse heart: An MR tagging study. *J Magnet Reson Imag.* 2008;27:1263-1270.

35. Young AA, French BA, Yang Z, Cowan BR, Gilson WD, Berr SS, Kramer CM, Epstein FH. Reperfused myocardial infarction in mice: 3D mapping of late gadolinium enhancement and strain. *J Cardiovasc Magn Reson.* 2006;8:685-692.

36. Costa KD, Takayama Y, McCulloch AD, Covell JW. Laminar fiber architecture and three-dimensional systolic mechanics in canine ventricular myocardium. *Am J Physiol Heart Circ Physiol.* 1999;276:H595-H607.

37. Matsubara I, Millman BM. X-ray diffraction patterns from mammalian heart muscle. *J Mol Biol.* 1974;82:527-536.

38. Rodriguez EK, Omens JH, Waldman LK, McCulloch AD. Effect of residual stress on transmural sarcomere length distributions in rat left ventricle. *Am J Physiol.* 1993;264(4 Pt. 2):H1048-H1056.

39. Williams CD, Regnier M, Daniel TL. Axial and radial forces of cross-bridges depend on lattice spacing. *PLoS Comput Biol.* 2010;6:e1001018.

40. Costa KD, Holmes JW, McCulloch AD. Modelling cardiac mechanical properties in three dimensions. *Phil Trans R Soc Lond A.* 2001;359:1233-1250.

41. Rademakers FE, Rogers WJ, Guier WH, Hutchins GM, Siu CO, Weisfeldt ML, Weiss JL, Shapiro EP. Relation of regional cross-fiber shortening to wall thickening in the intact heart. Three-dimensional strain analysis by NMR tagging. *Circulation.* 1994;89:1174-1182.

Chapter 4

General Conclusions

In the prestretch study, the effects of timing and magnitude of prestretch on developed twitch tension in mouse papillary muscles were investigated. Twitch tension and work performed by the muscle were highly dependent on the timing and magnitude of prestretch. A time-varying stiffness analysis made it clear that the stiffness change during contraction did have a substantial effect on the twitch tension, but it could not fully explain the results. The force-velocity relationship could help explain some of the results that could not be explained by the time-varying stiffness analysis. Shortening deactivation could explain some of the deactivating effect of prestretches occurring late in the twitch when there is little free calcium present. The analysis shows that time-varying stiffness alone cannot explain the effects of prestretch on twitch tension; other mechanisms such as force-velocity and shortening deactivation need to be included.

In the vinculin study, the effects of Vcl deletion and hence vinculin deficiency on sarcomeric structure were investigated, as well as the possible mechanistic link between sarcomere function and regional fiber mechanics in the intact mouse heart. cVclKO mice were studied before the onset of cardiac dysfunction focus on the effects of the deletion without the overwhelming additional effects of heart failure. The

experimental results along with the mechanistic model indicate that vinculin deficiency can have a direction-dependent effect on regional wall mechanics that can be explained by altered transverse stiffness and force development at the level of the crossbridge.

4.1 Mechanisms involved in explaining the effects of prestretch can be used when modeling physiological stretch

The work presented here demonstrates that the effects of prestretch on twitch tension can be explained by a combination of a time-varying stiffness, the force-velocity relation, and shortening-induced muscle deactivation. This information is of value because it brings forward the mechanisms that are most important in describing the effects of a stretch that has physiological duration, shape, and magnitude. While cardiac muscle mechanics is an intensely studied field, and there is endless information on the mechanics involved in muscle contraction, there is little that describes which mechanisms are totally necessary in describing the effects of a physiological stretch, such as prestretch. When modeling cardiac muscle contraction either in the whole heart or in isolated tissue, the model should be able to reproduce the crucial mechanisms uncovered here. Future work could involve developing a model that includes time-varying stiffness, the force-velocity relation, and shortening deactivation, and seeing how well it predicts the experimental results measured here.

4.2 Prestretch is a component of the work imbalance seen *in-vivo* in late-activated regions

Previous studies have concluded that asynchronously contracting hearts undergoing regional ventricular pacing have regions of external work imbalance. These studies showed that early-activated regions produced significantly less external work than late-activated regions. Observed imbalances in workload have been shown to play a role in asymmetrical hypertrophy. The results of the experimental studies shown here indicate that simulated prestretches with timing similar to the prestretch observed in late-activated regions *in-vivo* did more work than muscles that were not prestretched. This indicates that prestretch could contribute or be associated with the work imbalance observed in dyssynchronous activation. While it is known that there is an increase in work performed in late-activated regions, the role of prestretch in this increased workload has never been investigated (by our knowledge) until now. Future work could involve investigating how reducing prestretch could ultimately reduce the work imbalance observed in paced hearts.

4.3 A 2-dimensional crossbridge model is sufficient in determining force distributions

The crossbridge mechanics model used in the vinculin study was a 2-dimensional equivalent of the 3-dimensional structure of a crossbridge. The angle between the S2 segment and the thick filament (θ) was preserved from the 3-dimensional structure, and the lengths of the segments were scaled accordingly. The values from the 2-dimensional crossbridge model were then used to calculate stiffness

ratios at the scale of the lattice. The results from this work show that a more complicated 3-dimensional crossbridge geometry is not necessary when factoring in stresses at the scale of the lattice.

4.4 Mechanical analysis of changes at the scale of the lattice can be used to explain alterations in ventricular wall function

The work presented in the vinculin study shows how an analysis of the mechanics of a change at the scale of the lattice can be used to explain alterations at the tissue scale. This multi-scale approach shows how mechanical alterations at the subcellular level can impact function at the tissue scale. While this analysis gave insight into the effects of vinculin deletion, this same analysis can be applied to other disease models, given that there are other mutations of the costamere that have been implicated in dilated cardiomyopathy.

Appendix A

Detailed Methods of Myofilament Mechanics Model

A.1 Crossbridge Stiffness Analysis

The single spring stiffness K of the S2 domain in the cross-bridge model can be resolved into axial K_{ff} and radial K_{tt} component stiffnesses by using the force balance equations[1] to derive the change in the axial and radial force components (F_{ff} and F_{tt}) due to an infinitesimal change in the axial and radial displacement components in the strongly bound and strained state of the cross-bridge.

The forces acting along the S2 segment can be resolved as $F\sin\theta$ and $F\cos\theta$ along the radial and axial directions.

$$
\begin{aligned}
F_{tt} &= F\sin\theta \\
F_{ff} &= F\cos\theta \\
\frac{dF_{tt}}{d\theta} &= \frac{dF}{d\theta}\sin\theta + F\cos\theta \\
\frac{dF_{ff}}{d\theta} &= \frac{dF}{d\theta}\cos\theta - F\sin\theta
\end{aligned}
\qquad \text{[A.1]}
$$

Similarly, the displacements along the S2 segment can also be resolved into radial and axial components.

$$
\begin{aligned}
r &= l\sin\theta \\
x &= l\cos\theta \\
\frac{dr}{d\theta} &= \frac{dl}{d\theta}\sin\theta + l\cos\theta \\
\frac{dx}{d\theta} &= \frac{dl}{d\theta}\cos\theta - l\sin\theta
\end{aligned}
\qquad \text{[A.2]}
$$

From the definition of spring stiffness, $F = K(l_{S2} - \hat{l}_{S2})$, where $\hat{l}_{S2}$ is the rest length of the spring and l_{S2} is the strained length. For the radial stiffness, dx=0, giving $\frac{dl}{d\theta} = l\tan\theta$ and $\frac{dr}{d\theta} = \frac{l}{\cos\theta}$, and hence:

$$
\begin{aligned}
\frac{dF}{d\theta} &= \frac{dF}{dl}\frac{dl}{d\theta} = Kl\tan\theta \\
\frac{dF_{tt}}{d\theta} &= \frac{K(l - l_0\cos^2\theta)}{\cos\theta} \\
\frac{dF_{tt}}{dr} &= \frac{dF_{tt}}{d\theta}\frac{d\theta}{dr} \\
&= K\left(1 - \frac{l_0}{l}\cos^2\theta\right)
\end{aligned}
\qquad \text{[A.3]}
$$

Similarly, for the axial stiffness, dr=0, $\frac{dl}{d\theta} = \frac{-l}{\tan\theta}$ and $\frac{dx}{d\theta} = \frac{-l}{\sin\theta}$, resulting in:

$$\frac{dF}{d\theta} = \frac{dF}{dl}\frac{dl}{d\theta} = \frac{-Kl}{\tan\theta}$$
$$\frac{dF_{ff}}{d\theta} = \frac{-K(l - l_0 \sin^2\theta)}{\sin\theta}$$
$$\frac{dF_{ff}}{dx} = \frac{dF_{ff}}{d\theta}\frac{d\theta}{dx}$$
$$= K\left(1 - \frac{l_0}{l}\sin^2\theta\right) \qquad \text{[A.4]}$$

From these two equations, we get the ratio of radial to axial stiffness to be given in terms of the S2 segment angle and lengths by:

$$\frac{K_{tt}}{K_{ff}} = \frac{\left(l - l_0\cos^2\theta\right)}{\left(l - l_0\sin^2\theta\right)} \qquad \text{[A.5]}$$

A.2 Lattice Analysis

From the above analysis, the cross-bridges can be represented by equivalent fiber and transverse stiffnesses K_{ff} and K_{tt}, respectively. Assuming that the lattice is stretched in the perpendicular planes such that it deforms by u in both the axial (fiber) direction and the radial (transverse) direction, the energy stored due to deformation of a single spring structure is $\frac{1}{2}Ku^2$ where K is the stiffness in either the fiber or the transverse direction. There are six cross-bridges in each repeating hexagonal unit of the sarcomere (marked in yellow in Figure A1), leading to a total energy of $6\times\frac{1}{2}Ku^2$. The undeformed area of the hexagonal unit cell is with an axial length of α_0 is $\frac{3\sqrt{3}}{2}\Delta_0^2$.

This gives an energy density in the unit cell to be $\frac{1}{2}\left(\frac{4\sqrt{3}}{3}\right)\frac{K_a}{\alpha_0}\left(\frac{u}{\Delta_0}\right)^2$ in the fiber and $\frac{1}{2}\left(\frac{4\sqrt{3}}{3}\right)\frac{K_r}{\alpha_0}\left(\frac{u}{\Delta_0}\right)^2$ in the transverse directions, respectively.

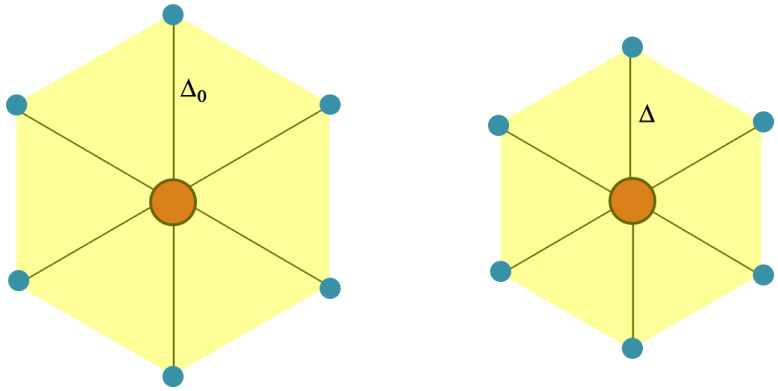

Figure A1: Isolated unit cell marked in yellow showing the actin and myosin filament cross-sections. The lattice spacing at rest is Δ_0. In the activated state, the lattice spacing is Δ

Consider an isolated hexagonal unit cell that is deformed due to stretching of the cross-bridges. The lattice spacing changes by a magnitude u in the radial direction. The initial width of the unit cell is $\sqrt{3}\Delta_0$, and after deformation this width becomes $\sqrt{3}(\Delta_0+u)$ or $\sqrt{3}\Delta$. Using a coordinate system with x_2 aligned with the unit cell width, the deformation gradient in the x_2 direction is $\left(1+\frac{u}{\Delta_0}\right)$. Similarly, the deformation gradient in the x_3 direction is $\left(1+\frac{u}{\Delta_0}\right)$.

The 2D deformation gradient tensor (**F**) and 2D finite strain tensor (**E**) can be expressed as

$$\mathbf{F} = \begin{bmatrix} 1+\dfrac{u}{\Delta_0} & 0 \\ 0 & 1+\dfrac{u}{\Delta_0} \end{bmatrix}$$

$$\mathbf{E} = \frac{1}{2}(\mathbf{F}^T\mathbf{F} - 1) = \begin{bmatrix} \dfrac{u}{\Delta_0}\left(1+\dfrac{u}{2\Delta_0}\right) & 0 \\ 0 & \dfrac{u}{\Delta_0}\left(1+\dfrac{u}{2\Delta_0}\right) \end{bmatrix} \qquad \text{[A.6]}$$

Similarly, in the axial direction, the deformation gradient is given by $\left(1+\dfrac{u}{\alpha_0}\right)$ and the strain $\mathbf{E_{11}}$ by $\dfrac{u}{\alpha_0}\left(1+\dfrac{u}{2\alpha_0}\right)$.

Assuming a linear strain energy relation, we can equate the strain energy in a unit cell to the energy from the deformation of the cross-bridges in the transverse direction as $W = \frac{1}{2}C_t(E_{22}^2 + E_{33}^2)$, assuming that the transverse material stiffness C_t is constant (transversely isotropic) in the plane perpendicular to the actin/myosin filaments. Substituting the strain values, we can equate the strain energy.

$$W = \frac{1}{2} 2C_t \left(\frac{u}{\Delta_0} \right)^2 \left(1 + \frac{u}{\Delta_0} + \frac{1}{4} \left(\frac{u}{\Delta_0} \right)^2 \right) = \frac{1}{2} \left(\frac{4\sqrt{3}}{3} \right) \frac{K_{tt}}{\alpha_0} \left(\frac{u}{\Delta_0} \right)^2$$

$$\Rightarrow C_t = \frac{2\sqrt{3}}{3\alpha_0 \left(1 + \frac{u}{\Delta_0} + \frac{1}{4} \left(\frac{u}{\Delta_0} \right)^2 \right)} K_{tt} \qquad \text{[A.7]}$$

This gives the relation to the transverse material stiffness as a function of the transverse cross-bridge stiffness K_{tt}, the lattice spacing Δ_0, the unit-cell axial spacing α_0, and the cross-bridge lengthening the in the plane, u. Since u is small, we can neglect the square term leading to a simpler relation, $C_t = \frac{2}{\sqrt{3}} \frac{1}{\alpha_0} \frac{\Delta_0}{\Delta} K_{tt}$ where Δ is the deformed lattice spacing.

In the axial fiber direction, $W = \frac{1}{2} C_f E_{33}^2$ and again equating the energy in the axial direction, we obtain:

$$W = \frac{1}{2} C_f \left(\frac{u}{\alpha_0} \right)^2 \left(1 + \frac{u}{\alpha_0} + \frac{1}{4} \left(\frac{u}{\alpha_0} \right)^2 \right) = \frac{1}{2} \left(\frac{4\sqrt{3}}{3} \right) \frac{K_{ff}}{\alpha_0} \left(\frac{u}{\Delta_0} \right)^2$$

$$\Rightarrow C_f = \frac{4\sqrt{3}}{3\alpha_0 \left(1 + \frac{u}{\alpha_0} + \frac{1}{4} \left(\frac{u}{\alpha_0} \right)^2 \right)} \left(\frac{\alpha_0}{\Delta_0} \right)^2 K_{ff} \qquad \text{[A.8]}$$

which, upon linearization, yields $C_f = \frac{4}{\sqrt{3}} \frac{1}{\alpha} \left(\frac{\alpha_0}{\Delta_0} \right)^2 K_{ff}$ and the macroscopic lattice stiffness stiffness ratio can be computed to be $\frac{C_t}{C_f} = \frac{1}{2} \left(\frac{\Delta_0}{\alpha_0} \right)^3 \frac{\alpha}{\Delta} \frac{K_{tt}}{K_{ff}}$.

The stress in the axial direction can be computed as $\sigma_{ff} = C_f E_{11}$ and in the transverse direction to be $\sigma_{tt} = C_r E_{22}$. This reduces to

$$\sigma_{ff} = \frac{4\sqrt{3}}{3\alpha_0 \left(1 + \frac{u}{\alpha_0} + \frac{1}{4} \left(\frac{u}{\alpha_0} \right)^2 \right)} \left(\frac{\alpha_0}{\Delta_0} \right)^2 K_{ff} \frac{u}{\alpha_0} \left(1 + \frac{u}{2\alpha_0} \right)$$

$$= \frac{4\sqrt{3} u \alpha_0}{3 \left(\alpha_0 + \frac{u}{2} \right)} \left(\frac{1}{\Delta_0} \right)^2 K_{ff} \qquad \text{[A.9]}$$

Similarly in the transverse direction

$$\sigma_{tt} = \frac{2\sqrt{3} u}{3\alpha_0 \left(\Delta_0 + \frac{u}{2} \right)} K_{tt} \qquad \text{[A.10]}$$

and the transverse to fiber macroscopic peak systolic stress ratio is:

$$\frac{\sigma_{tt}}{\sigma_{ff}} = \frac{\dfrac{2\sqrt{3}u}{3\alpha_0\left(\Delta_0 + \dfrac{u}{2}\right)}K_{tt}}{\dfrac{4\sqrt{3}u\alpha_0}{3\left(\alpha_0 + \dfrac{u}{2}\right)}\left(\dfrac{1}{\Delta_0}\right)^2 K_{ff}} = \frac{1}{2}\left(\frac{\Delta_0}{\alpha_0}\right)^2 \frac{\left(\alpha_0 + \dfrac{u}{2}\right)}{\left(\Delta_0 + \dfrac{u}{2}\right)}\frac{K_{tt}}{K_{ff}}$$

$$\approx \frac{1}{2}\left(\frac{\Delta}{\alpha}\right)\frac{K_{tt}}{K_{ff}} \qquad \text{[A.11]}$$

Since the axial length of the unit cell α is equal to the cross-bridge axial length δ, we get the stress ratio to be

$$\frac{\sigma_{tt}}{\sigma_{ff}} \approx \frac{1}{2}\left(\frac{\Delta}{\delta}\right)\frac{K_{tt}}{K_{ff}} \qquad \text{[A.12]}$$

A.3 Ventricular Mechanics Model

Table A1. Parameters used in the micromechanical and finite element models

Parameter	Description	WT Value	cVclKO Value	Units	Source
k_spr	S2 spring constant	2	2	pN/nm	[10]
$\hat{l}_{s2}$	Unloaded S2 spring length	15	15	nm	*
l_{S2}	S2 resting length	18	18	nm	**
l_{S1}	S1 Length (projected)	11.3	11.3	nm	[1]
α	Axial angle of Attachment	45	45	deg	[1],[4]
Rm	radius of myosin	5.5	5.5	nm	[5]
Ra	radius of actin	3	3	nm	[5]
δ	Axial distance of 3 myosin head pairs	43.5	43.5	nm	[6]
V_s	Volume constant	1620	2030	nm*μm	EM Meas.
SL_unloaded	Relaxed unloaded sarcomere length	1.88	1.74	um	EM Meas.
SL_sys	Contracted unloaded sarcomere length	1.5	1.43	um	EM Meas.
S_f	EM shrinkage factor	1.2	1.2	n/a	[7]
Finite Element Model Parameters					
C	Stress scaling coefficient	0.88	0.88	n/a	[8]
bf	Fiber strain coefficient	18.5	18.5	n/a	[8]
bt	Transverse strain coefficient	3.58	3.58	n/a	[8]
bfs	Fiber-transverse-shear coefficient	1.63	1.63	n/a	[8]
bulk_mod	Bulk modulus	250	250	kPa	[9]
bcl	Basic cycle length	600	600	ms	[9]
bten	Governs shape of peak isometric tension-SL relation	1.8	1.8	1/μm	[9]
c0max	Maximum intracellular calcium concentration	4.35	4.35	μM	[8]
c0	Peak intracellular calcium concentration	4.35	4.35	μM	[8]
tmax	Isometric tension under maximal activation	137.5	137.5	kPa	[8]
dur	Scales duration of contraction	0.25	0.25	n/a	[9]
rmc	Slope of twitch contraction	52.49	52.49	ms/μm	[9]
bc	Offset of twitch contraction	55.26	55.26	ms	[9]
rmr	Slope of twitch relaxation	131.2	131.2	ms/μm	[9]
br	Offset of twitch relaxation	-94.34	-94.34	ms	[9]
c_act	Arbitrary stress scaling factor	121	121	n/a	

** Parameter value derived from projections of a 3-dimensional model using values from [10], to the 2-dimensional model that is used here.

* Parameter value derived from new 2-dimensional model lengths.

REFERENCES

1. Schoenberg M. Geometrical factors influencing muscle force development: I. The effect of filament spacing upon axial forces. *Biophys J.* 1980;30:51-68.

2. Matsubara I, Millman BM. X-ray diffraction patterns from mammalian heart muscle. *J Mol Biol.* 1974;82:527-536.

3. Rayment I, Holden HM, Whittaker M, Yohn CB, Lorenz M, Holmes KC, Milligan RA. Structure of the actin-myosin complex and its implications for muscle contraction. *Science.* 1993;261:58-65.

4. Julian FJ, Moss RL, Sollins MR. The mechanism for vertebrate striated muscle contraction. *Circ Res.* 1978;42:2-14.

5. Sonnenblick EH, Skelton CL. Reconsideration of the ultrastructural basis of cardiac length-tension relations. *Circ Res.* 1974;35:517-526.

6. Craig R, Woodhead JL. Structure and function of myosin filaments. *Curr Opin Struct Biol.* 2006;16:204-212.

7. Millman BM. The filament lattice of striated muscle. *Physiol Rev.* 1998;78:359-391.

8. Guccione JM, Waldman LK, McCulloch AD. Mechanics of active contraction in cardiac muscle. *J Biomech Eng.* 1993;115(1):72-90.

9. Kerckhoffs RC, Neal ML, Gu Q, Bassingthwaighte JB, Omens JH, McCulloch AD. Coupling of a 3D finite element model of cardiac ventricular mechanics to lumped systems models of the systemic and pulmonic circulation. *Ann Biomed Eng.* 2007;35(1):1-18.

10. Williams CD, Regnier M, Daniel TL. Axial and radial forces of cross-bridges depend on lattice spacing. *PLoS Comput Biol.* 2010;6:e1001018.